The Astrophysical Journal, 850:66 (26pp), 2017 November 20 https://doi.org/10.3847/1538-4357/aa937d

AGN Populations in Large-volume X-Ray Surveys: Photometric Redshifts and Population Types Found in the Stripe 82X Survey

Tonima Tasnim Ananna[1,2], Mara Salvato[3], Stephanie LaMassa[4], C. Megan Urry[1,2,5], Nico Cappelluti[1,2], Carolin Cardamone[6], Francesca Civano[7], Duncan Farrah[8], Marat Gilfanov[9,10], Eilat Glikman[11], Mark Hamilton[12], Allison Kirkpatrick[1,2], Giorgio Lanzuisi[13,14], Stefano Marchesi[15], Andrea Merloni[3], Kirpal Nandra[3], Priyamvada Natarajan[2,5], Gordon T. Richards[16], and John Timlin[16]

[1] Department of Physics, Yale University, P.O. Box 201820, New Haven, CT 06520-8120, USA
[2] Yale Center for Astronomy and Astrophysics, P.O. Box 208121, New Haven, CT 06520, USA; tonimatasnim.ananna@yale.edu
[3] MPE, Giessenbachstrasse 1, D-85748, Garching, Germany
[4] Space Telescope Science Institute, 3700 San Martin Dr., Baltimore, MD 21218, USA
[5] Department of Astronomy, Yale University, P.O. Box 208101, New Haven, CT 06520, USA
[6] Department of Math & Science, Wheelock College, Boston, MA 02215, USA
[7] Harvard-Smithsonian Center for Astrophysics, 60 Garden Street, Cambridge, MA 02138, USA
[8] Department of Physics, Virginia Tech, Blacksburg, VA 24061, USA
[9] Max-Planck Institut fuer Astrophysik, Karl-Schwarzschild-Str. 1, Postfach 1317, D-85741 Garching, Germany
[10] Space Research Institute of Russian Academy of Sciences, Profsoyuznaya 84/32, 117997 Moscow, Russia
[11] Department of Physics, Middlebury College, Middlebury, VT 05753, USA
[12] Yale University, USA
[13] Dipartimento di Fisica e Astronomia, Universitá di Bologna, Via Gobetti 93/2, I-40129 Bologna, Italy
[14] INAF—Osservatorio Astronomico di Bologna, Via Gobetti 93/3, I-40129 Bologna, Italy
[15] Department of Physics & Astronomy, Clemson University, Clemson, SC 29634, USA
[16] Department of Physics, Drexel University, 32 S. 32nd Street, Philadelphia, PA 19104, USA
Received 2017 July 28; revised 2017 September 30; accepted 2017 October 10; published 2017 November 17

Abstract

Multiwavelength surveys covering large sky volumes are necessary to obtain an accurate census of rare objects such as high-luminosity and/or high-redshift active galactic nuclei (AGNs). Stripe 82X is a 31.3 X-ray survey with *Chandra* and *XMM-Newton* observations overlapping the legacy Sloan Digital Sky Survey Stripe 82 field, which has a rich investment of multiwavelength coverage from the ultraviolet to the radio. The wide-area nature of this survey presents new challenges for photometric redshifts for AGNs compared to previous work on narrow-deep fields because it probes different populations of objects that need to be identified and represented in the library of templates. Here we present an updated X-ray plus multiwavelength matched catalog, including *Spitzer* counterparts, and estimated photometric redshifts for 5961 (96% of a total of 6181) X-ray sources that have a normalized median absolute deviation, $\sigma_{\rm nmad} = 0.06$, and an outlier fraction, $\eta = 13.7\%$. The populations found in this survey and the template libraries used for photometric redshifts provide important guiding principles for upcoming large-area surveys such as *eROSITA* and 3*XMM* (in X-ray) and the Large Synoptic Survey Telescope (optical).

Key words: catalogs – quasars: absorption lines – quasars: emission lines – quasars: general – techniques: photometric – techniques: spectroscopic

Supporting material: FITS file

1. Introduction

Over the last two decades, X-ray surveys have been a major tool for advancing our understanding of galaxies and black hole growth (e.g., Brandt & Hasinger 2005). The most massive black holes in the most massive galaxies are particularly interesting because, although they are rare, population synthesis models suggest that they may account for more than half of the total mass enclosed in black holes (e.g., Treister et al. 2009; Ueda et al. 2014; Buchner et al. 2015). Massive galaxies and black holes are also likely to have formed early and grown rapidly at or above the Eddington rate (Yu & Tremaine 2002; Hopkins et al. 2006; van Dokkum et al. 2010; Du et al. 2015). It is therefore important that any complete census of black hole growth include high-luminosity and/or high-redshift active galactic nuclei (AGNs)—i.e., quasars—which means surveying a large enough volume to find these relatively rare objects.

To date, most quasars have been found in wide-area, large-volume optical surveys such as the Sloan Digital Sky Survey (SDSS), which preferentially selects AGNs that are unobscured by circumnuclear or galactic-scale dust. Soft X-ray surveys like *ROSAT* (0.1–2.4 keV) cover even larger areas but are also insensitive to obscured AGNs. In contrast, infrared and hard X-ray (2–10 keV) observations can recover obscured or reddened AGNs missed by optical surveys (Brandt & Hasinger 2005; Cardamone et al. 2008; Donley et al. 2012; Mendez et al. 2013; Kirkpatrick et al. 2015; Del Moro et al. 2016). However, while infrared surveys can efficiently select the most luminous obscured AGNs (Lacy et al. 2004; Stern et al. 2012; Assef et al. 2013; Kirkpatrick et al. 2013), at fainter fluxes, star-forming galaxies are a significant contaminant, and a large fraction of AGNs can be missed altogether (e.g., Donley et al. 2010; Mendez et al. 2013).

Hard X-ray surveys efficiently find both unobscured and obscured AGNs at a range of luminosities. The moderate-luminosity AGNs found in deep and medium-deep X-ray surveys like the *Chandra* Deep Fields (Alexander et al. 2003; Lehmer et al. 2005; Comastri et al. 2011; Xue et al. 2011; Luo et al. 2017), COSMOS (Hasinger et al. 2007; Cappelluti et al. 2009; Brusa et al. 2010; Civano et al. 2016; Marchesi et al. 2016), and All-Wavelength Extended Groth Strip International Survey (AEGIS; Nandra et al. 2015) have an intrinsic obscured-to-unobscured ratio of roughly 3:1 (Treister et al. 2004; Buchner et al. 2015), and the higher-energy *Swift*/BAT (Baumgartner et al. 2013) X-ray survey shows a similar obscured fraction, ∼70%, in the local universe (Ricci et al. 2015), suggesting that obscured black hole growth may dominate overall. Theories of black hole growth in quasars also imply an extended phase of obscured accretion (Sanders et al. 1988; Hopkins et al. 2006).

However, this mix of information leaves unclear the question of whether there is a substantial population of obscured AGNs at high luminosity and/or redshift, because small-volume X-ray surveys do not sample high-luminosity quasars. Fortunately, large-volume hard X-ray surveys sensitive enough to yield large numbers of quasars and with sufficient multiwavelength data to study black hole accretion and star formation rate in the host galaxy are now becoming available (e.g., *Chandra* Boötes, 10 deg^2, Murray et al. 2005; Stern et al. 2012; *XMM*-XXL, ∼50 deg^2, Menzel et al. 2016; Pierre et al. 2016; Georgakakis et al. 2017; *XMM*-LSS, 11.1 deg^2, Pierre et al. 2007; Chiappetti et al. 2013; Stripe 82X, 31.3 deg^2, *XMM* + *Chandra*, LaMassa et al. 2013a, 2013b, 2016b). Stripe 82X is among the largest of these hard X-ray surveys, with the most extensive multiwavelength data (millimeter, ACT, Battaglia et al. 2016; radio, FIRST, VLA, Becker et al. 1995; Hodge et al. 2011; ultraviolet, *Galaxy Evolution Explorer* (*GALEX*), Martin et al. 2005; optical, SDSS, Annis et al. 2014; Jiang et al. 2014; Fliri & Trujillo 2016; near-infrared, Vista Hemispherical Survey (VHS), United Kingdom Infrared Telescope (UKIRT) Infrared Deep Sky Survey (UKIDSS), Lawrence et al. 2007; McMahon et al. 2013; mid-infrared, *Wide-field Infrared Survey* (*WISE*), *Spitzer*, Stern et al. 2012; Papovich et al. 2016; Timlin et al. 2016; far-infrared, *Herschel*, Viero et al. 2014). It also has extensive spectroscopy (Strauss et al. 2002; Jones et al. 2004, 2009; Garilli et al. 2008; Croom et al. 2009; Drinkwater et al. 2010; Coil et al. 2011; Ahn et al. 2012, 2014; Newman et al. 2013; SDSS Collaboration et al. 2016), including our own work with WIYN, Palomar, and Keck (LaMassa et al. 2016b, hereafter LM16). Nearly one-third of the Stripe 82X sources have spectroscopic redshifts used in this work, and the SDSS-IV eBOSS program (Abolfathi et al. 2017) will raise the spectroscopic completeness to 43%.

Previously, accurate photometric redshifts were obtained for X-ray samples from small, deep surveys like *XMM*-COSMOS (2.13 deg^2; Salvato et al. 2009, hereafter S09), the *Chandra* Deep Field–South (CDFS, 0.13 deg^2; Luo et al. 2010; Hsu et al. 2014), the Extended *Chandra* Deep Field–South (ECDFS, 0.3 deg^2; Cardamone et al. 2010; Hsu et al. 2014), *Chandra*-COSMOS (0.90 deg^2; Salvato et al. 2011, hereafter S11), *Chandra*-COSMOS-Legacy (2.2 deg^2; Civano et al. 2016; Marchesi et al. 2016), the Lockman Hole (0.20 deg^2; Fotopoulou et al. 2012), and AEGIS (0.67 deg^2; Nandra et al. 2015). But the populations probed in these narrow-deep surveys were different from the X-ray-bright sample of wider and shallower surveys such as Stripe 82X.

In this paper, we identified a list of templates appropriate for wider and shallower X-ray survey samples with higher-luminosity AGNs with which we obtain photometric redshifts with an accuracy comparable to that of some of the deeper surveys. Not only does this make the Stripe 82X sample valuable, it also provides an initial calibration for surveys of comparable depth, such as Boötes, *XMM*-XXL, and the upcoming *eROSITA* All-Sky survey (Merloni et al. 2012). This work will also be relevant in calculating photometric redshifts for AGNs in large-scale non-X-ray surveys such as the Large Synoptic Survey Telescope (LSST; Ivezic et al. 2008).

The paper is organized as follows. In Section 2, we describe the Stripe 82X data; we also explain the multiwavelength catalog matching, with details about how ambiguous associations were resolved. The procedures used to calibrate the photometric redshifts, which closely follow those of S09 and S11, are described in Section 3. In Section 4, we present the final photometric redshifts, along with a preliminary characterization of the sources and some conclusions about calculating photometric redshifts for a large-volume X-ray survey using broadband data. In Section 5, we summarize the key results of this work. Appendix A describes the final Stripe 82X multiwavelength catalog and redshifts. Appendix B describes our process for selecting the set of templates used in fitting for photometric redshifts with an example, and Appendix C details how we calculated X-ray-to-optical flux ratios.

2. Identifying Multiwavelength Counterparts of Stripe 82 X-Ray Sources

2.1. Characteristics of the Stripe 82X Population

Figure 1 shows the regions covered by the Stripe 82X survey. There are two regions with contiguous *XMM-Newton* coverage awarded to our team in *XMM-Newton* cycles 10 and 13 (AO10 and AO13), and the rest are from archival *XMM-Newton* and *Chandra* pointings, as described in LaMassa et al. (2013a, 2013b, 2016b). The AO10 and AO13 surveys have slightly different exposure times: 6–8 ks for AO13 and 4–6 ks for AO10. The nonuniform exposure times occur due to mosaicking. Key ancillary data sets are indicated in the figure (see caption for details).

The brighter flux limit of Stripe 82X presents several challenges. First, the flux distribution of the AGN population sampled by Stripe 82X is not well represented in pencil-beam surveys for which photometric redshifts have been computed in previous works. Figure 2 shows histograms of soft X-ray flux (0.5–2 keV) for deeper, smaller-volume surveys compared to Stripe 82X. The bright AGNs typically found in Stripe 82X are rare in COSMOS and practically absent in the CDFS.

Conversely, the bottom panel of Figure 2 shows that *eROSITA* is expected to have a flux limit similar to that of our *XMM-Newton* AO10 and AO13 surveys. Photometric redshifts for other large-volume X-ray surveys, such as the 3*XMM* Serendipitous Catalog (880 deg^2; Rosen et al. 2016) and the *Chandra* Source Catalog, are not available yet, but the object types will likely be similar to those of Stripe 82X.

We resolve the first challenge by selecting a reduced set of templates that represents the population of Stripe 82X, as

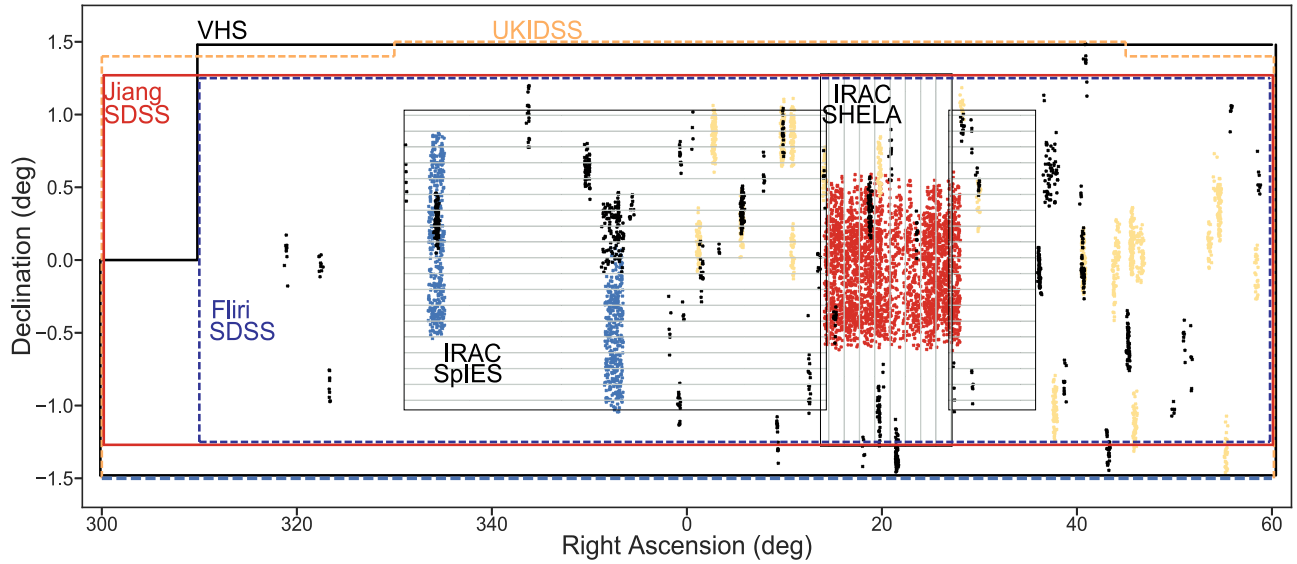

Figure 1. Map of the Stripe 82X survey, along with the footprint of multiwavelength coverage. Note that the vertical extent of the plot is ∼2.°5, and the horizontal extent is 120°. The dots represents X-ray sources: AO13 (red), AO10 (blue), archival *XMM-Newton* sources (yellow), and *Chandra* sources (black). The solid red line and the dark blue dashed line encompass areas covered by two SDSS coadded optical catalogs, Jiang et al. (2014) and Fliri & Trujillo (2016), respectively. The solid black line delineates the area covered by the NIR VHS (McMahon et al. 2013), and the yellow dashed line is the area covered by UKIDSS (Lawrence et al. 2007, NIR). The patches with horizontal and vertical lines show areas covered by the mid-infrared *Spitzer* Infrared Array Camera Equatorial Survey (Timlin et al. 2016) and *Spitzer*-HETDEX Exploratory Large Area Survey (Papovich et al. 2016), respectively. Not explicitly shown in this map are *WISE* and *GALEX*, which cover the whole sky. As explained later, we do not use *GALEX* or UKIDSS data to identify multiwavelength counterparts of X-ray sources, although we do add data from these surveys to construct spectral energy distributions.

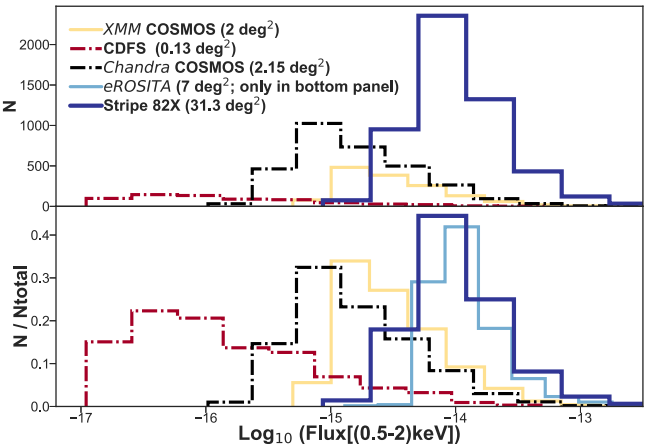

Figure 2. Soft X-ray flux distributions for point-like sources in several X-ray surveys. Top panel: absolute number of sources in each survey. Bottom panel: each survey is normalized to the total number of sources in that survey. The bright sources that dominate Stripe 82X are barely present in the deep pencil-beam surveys. This is why the library of spectral energy distribution templates for computing photometric redshifts must be optimized. The *eROSITA* histogram in the bottom panel was estimated using contiguous 7 deg^2 *XMM*-XXL data (Liu et al. 2016; Menzel et al. 2016; Georgakakis et al. 2017) cut at the fluxes expected for *eROSITA*.

described in Section 3.2 and Appendix B. These templates should also be applicable to the other wide shallow fields, such as 3*XMM* and *eROSITA*. In fact, the template library we compiled for this work has already been used successfully in Georgakakis et al. (2017) to calculate photometric redshifts for *XMM*-XXL sources (50 deg^2; Menzel et al. 2016) with X-ray fluxes (soft band) $F_X < 10^{-13}$ erg s^{-1} cm^{-2}.

The second challenge is that Stripe 82X contains both archival observations of varying depths—6 deg^2 from *Chandra* and 7.4 deg^2 from *XMM-Newton* (LaMassa et al. 2013a, 2013b, 2016b)—and relatively uniform *XMM-Newton* imaging awarded to our team in AO10 and AO13 (PI: Urry; LaMassa et al. 2013a; LM16). After removing periods of high background, the latter allocations resulted in 4.6 and 15.6 deg^2 of independent area, respectively. We dealt with the varying depths by calibrating each subsample separately for each field, i.e., optimizing the spectral energy distribution (SED) libraries independently, but in any case we converged on the same set of templates for all four fields (Section 3.2).

The third challenge is that for areas covering more than a few square degrees with a variety of observations taken by independent teams with different instruments, multiwavelength catalogs are assembled by simple matches in position. Instead, for smaller fields, such as COSMOS (S09; S11; Hsu et al. 2014), CANDELS GOODS-S (Guo et al. 2013), and ECDFS MUSYC (Cardamone et al. 2010), the multiwavelength catalogs are obtained in a homogeneous manner, including the registration of the images at the same reference and taking into account the individual point-spread function (PSF). For Stripe 82X, we had to reach a compromise while dealing with catalogs that have different types of fluxes or magnitudes (e.g., aperture-corrected, Petrosian) and very different spatial resolution, which is discussed further in Section 3.4.

2.2. Generating a New Stripe 82X Multiwavelength Catalog

A common challenge for all the X-ray surveys is finding the correct and consistent multiwavelength counterpart of each X-ray source. LM16 presented a combined multiwavelength catalog for all Stripe 82 X-ray fields, with identifications done pairwise using a statistical maximum likelihood estimator (MLE; described in detail in Section 2.3) algorithm (Sutherland & Saunders 1992). That is, each ancillary data set (*GALEX*, SDSS, VHS, UKIDSS, AllWISE) was matched separately to the master X-ray catalog. Once the counterpart was found, a

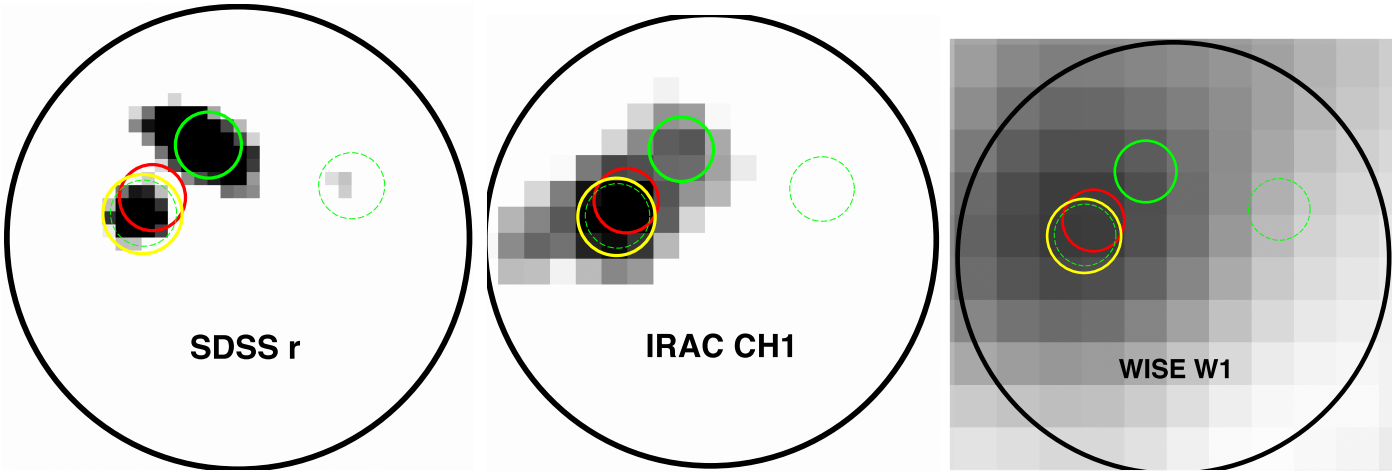

Figure 3. From left to right: field of Stripe 82X *XMM-Newton* source ID 2794 from LM16 (solid black circle with radius 7″) at the optical SDSS *r* band, near-infrared IRAC Ch1 (3.6 μm), and AllWISE W1 (3.4 μm). The positional errors for SDSS, VHS, and IRAC are only a few milliarcseconds; for clarity, we use bigger circles to indicate the location of the source in each band: a dashed green circle with radius 1″ around the SDSS *r* band, a solid yellow circle with radius 1.″2 for the VHS *K* band, and a solid red circle with radius 1″ for the IRAC CH1 source positions. In this example, the most likely optical counterpart from the MLE analysis (left) is the bright source at the top (solid green circle), but the infrared images suggest a more reliable counterpart below and to the left. The dashed green circles indicate other nearby optical sources that have a lower reliability match. We identify the source circled in yellow as the correct counterpart, which is the most likely counterpart according to VHS and IRAC but more accurately pinpointed by VHS.

match in coordinates was performed for retrieving radio and infrared information.

In LM16, running MLE on each band returned the same counterpart across multiwavelength catalogs for approximately 4943 (80%) cases. If we only consider the catalogs/wavebands that this work and LM16 have in common—*GALEX*, SDSS, VHS, UKIDSS, and AllWISE—487 (8%) X-ray sources in LM16 have conflicting associations (i.e., distinctly different sources are chosen as counterparts in different bands; see Figure 3 for an example). In such cases, LM16 left it to the reader to decide which ancillary band provides the correct X-ray counterpart. We note that LM16 found no associations for 12% of the sample because the potential counterparts were below an empirically determined reliability threshold (10%) or because no candidate counterparts were found within the search radius around the X-ray source (2%).

In this paper, we update the multiwavelength catalog, based in part on deeper and more homogeneous ancillary data than were previously available. Specifically, using new SDSS coadded catalogs from Fliri & Trujillo (2016; hereafter FT16) and MIR data from *Spitzer* (Papovich et al. 2016; Timlin et al. 2016), we repeated the MLE matching (for a detailed description of the process, see Section 2.3). Then, in cases of conflicting counterparts at different wavelengths, we established a procedure for identifying the same, correct counterpart at each wavelength (see Section 2.5), which is necessary if we are to use the SED to calculate photometric redshifts.

The optical data are from SDSS, which repeatedly imaged a 300 deg^2 area in the *u*, *g*, *r*, *i*, and *z* broadband filters, with 70–90 exposures at each location. The SDSS single-epoch images were combined to create deeper coadded catalogs (FT16; Jiang et al. 2014, hereafter J14) that reach ∼2.5 mag deeper than the single-epoch data (or the depth of the larger SDSS survey) and increase the likelihood of finding an optical association for an X-ray source. The FT16 catalog is 0.2 mag deeper in the SDSS *i* band than the earlier J14 coadded catalog because it eliminates data of poor quality. We use FT16 when available and J14 when the X-ray source is outside the footprint of the FT16 catalog.

We use near-infrared (NIR) data from the VHS (McMahon et al. 2013), which primarily covers the southern hemisphere but includes Stripe 82 (the equatorial coverage goes up to a declination of +1.°5). VHS has a 5σ K_{AB} depth of 20.3 mag and provides broadband data in the *J*, *H*, and *K* filters. We also use UKIDSS (Lawrence et al. 2007) NIR data when constructing SEDs, but not in the phase of counterpart identification (explained in Section 2.8).

MIR data comes from the *WISE* AllWISE catalog and the *Spitzer Space Telescope* Infrared Array Camera (IRAC). These two instruments have slightly different broadband filters that cover approximately the same wavelengths in the first two channels. AllWISE has a resolution of 1.″875 pixel^{-1} and 95% completeness at a depth of 19.8 mag (AB) at 3.4 μm.[17] This means that nearby objects are often blended together, and the positional accuracy is lower than that for VHS and SDSS. IRAC has much better spatial resolution than AllWISE (0.″8 pixel^{-1} in CH1 at 3.6 μm).

The *Spitzer* IRAC Equatorial Survey (SpIES) catalog (Timlin et al. 2016) has a 95% completeness at ∼20.34 mag (AB) in CH1. In the same band, the *Spitzer*-HETDEX Exploratory Large Area Survey (SHELA) catalog (Papovich et al. 2016) has a 95% completeness at 20.0 mag (AB). Because of their depth and resolution, for determining the counterparts, we use IRAC data rather than AllWISE when possible.

2.3. Running MLE on Optical and IR data

The MLE has been used to identify the correct association between sources from different catalogs, in particular for counterparts to point-like X-ray sources (e.g., Brusa et al. 2007; Georgakakis & Nandra 2011; Rovilos et al. 2011; Xue et al. 2011; Civano et al. 2012; LaMassa et al. 2013a, 2016b; Nandra et al. 2015; Marchesi et al. 2016). In this work, we highlight the major steps of the matching procedure, while the

[17] http://wise2.ipac.caltech.edu/docs/release/allwise/expsup/sec2_4a.html

Table 1
Number of X-ray Sources with Counterparts Identified in Ancillary Catalogs

	AO13	AO10	Archival *XMM*	Archival *Chandra*	Total
Area (deg^2)	15.6	4.6	7.4	6	31.3[a]
X-ray exposure time range (ks)	6–8	4–8	17–65	5.7–71.2	...
Number of X-ray sources[b]	2862	751	1607	1146	6366
Unique sources	2820	721	1496	1144	6181
Total number of multiwavelength associations[c]	2812 (99%)	716 (99%)	1453 (97%)	1063 (93%)	6044 (97.8%)
Number of associations common with LM16[d]	2555 (91%)	633 (88%)	1230 (82%)	911 (80%)	5329 (86%)
Changed association[e]	23 (0.8%)	5 (0.7%)	7 (0.5%)	5 (0.4%)	40 (0.6%)
New associations[f]	172 (6%)	57 (8%)	165 (11%)	113 (10%)	507 (8%)
Sub-threshold new associations	54 (2%)	17 (2%)	48 (3%)	32 (3%)	151 (2%)
Number with spectra	820 (29%)	270 (37%)	435 (29%)	361 (32%)	1886 (30%)

Notes.
[a] Nonoverlapping area.
[b] The number of sources detected in different X-ray bands at a 4.5σ level is given in Table 3 of LM16.
[c] Among unique sources.
[d] LM16 reports the best match of the X-ray sources to each multiwavelength band, but for 8% of those counterparts, not all bands agree on a single counterpart (e.g., the best NIR counterpart is different from the optical or ultraviolet counterpart). We resolve these ambiguities (Section 2.5), so here we report the number of our counterparts that lie within $1''$ of an LM16 counterpart in any band. We are only considering SDSS, VHS, and AllWISE associations from LM16 for this comparison, as these are the catalogs in which we look for associations.
[e] Compared to LM16.
[f] Not present in LM16. In this row, we ignore the sub-threshold associations in this catalog, as LM16 ignores sub-threshold associations.

reader can refer to the more detailed description in Naylor et al. (2013).

We performed MLE matching for six different optical, NIR, and MIR catalogs; the total number of matches for each catalog is given in Table 1. The MLE method considers three factors of the ancillary waveband to determine correct counterparts to the X-ray sources: (i) the area-normalized density of background sources in the field as a function of magnitude (or flux), (ii) the area-normalized density of sources in the vicinity of the X-ray source per unit magnitude after subtracting the background distribution, and (iii) the positional errors associated with each catalog (astrometric offsets between catalogs must be corrected in advance).

The most critical point is the estimate of the magnitude distribution of the background sources, so that we can distinguish between background sources and X-ray counterparts. For example, an oversubtraction of sources in point (ii) will reduce the likelihood that a faint source is identified as the right counterpart to an X-ray source, with the effect being stronger for shallow X-ray surveys like Stripe 82X. Also, many of the Stripe 82 counterparts will be stars, bright nearby objects, or quasars, which will outshine some fainter sources, reducing the effective depth (i.e., this part of the sky will appear shallower than other, random locations in the sky lacking bright objects). To put it another way, the background near our X-ray objects has fewer visible faint sources than the field as a whole, so the background estimated from elsewhere has more faint objects than the region of interest. This was already noticed by Rutledge et al. (2000) and Brusa et al. (2007) and is further explained in Naylor et al. (2013).

To mitigate the inaccuracy at faint magnitudes in Stripe 82, we use the following process. First, we find all the objects close to the X-ray positions, i.e., within circles of radius $5''$ for *Chandra* fields or $7''$ for *XMM-Newton* fields; this includes the true counterparts plus the background. The area-normalized histogram of the magnitudes of these objects is what we call the total magnitude distribution. Then, we estimate a preliminary area-normalized background tallying all the objects in a 2 deg^2 X-ray surveyed area. The total magnitude distribution includes fewer sources, is noisier, and has fewer objects than the estimated background at faint magnitudes. Therefore, we replace the total magnitude distribution at $r > 23.5$ mag with the estimated background at those faint magnitudes. Using these two distributions, we tentatively identify the counterparts of all the X-ray sources using the MLE method. We then refine the background estimate by removing a circle of $2''$ radius around each counterpart in the 2 deg^2 area (a few hundred sources) and repeat the counterpart identification. The magnitude distribution of these counterparts will be correct at the bright end but does not include objects fainter than $r = 23.5$ mag because they are considered background objects.

We still need to determine the background at faint magnitudes. We define a control sample of 18,000–20,000 objects with the same magnitude distribution as the bright counterparts (this is the distribution of counterpart magnitudes with $r < 23.5$ mag identified in the previous step) but located far enough away from the X-ray source positions to not be counterparts (though still in the X-ray surveyed region). We then measure the background near these objects within an annulus of inner radius $1''$ and outer radius $5''$ (for *Chandra* fields) or $7''$ (for *XMM-Newton* fields) around these objects. This empirically measures the background in regions where faint objects are masked by bright objects, similar to what occurs around X-ray sources. This corrected background agrees with the previously estimated background at bright magnitudes but no longer exceeds the total magnitude distribution at faint magnitudes (at $r \gtrsim 23$ mag). We refer to Section 2.2 in Brusa et al. (2007) for a demonstration.

We then repeat the identification process using the corrected background and the original total magnitude distribution. In addition, we make an astrometric correction by finding the median offset between the X-ray and ancillary catalogs and correcting the X-ray position after each iteration of the MLE identification (following Hsu et al. 2014). Typical offsets between X-ray and SDSS coordinates are $\sim 1''$ for *XMM-Newton* and $\sim 0\farcs02$ for *Chandra*. In the final output catalog, we

provide the original R.A. and decl. of the X-ray sources without the offsets applied.

As discussed above, we use the FT16 coadded SDSS catalog ($r < 25$ mag) where possible; otherwise, we use the J14 coadded catalog (*u, r,* and *z* bands). For the NIR, we use the VHS *K* band (McMahon et al. 2013), as it is deeper than UKIDSS and has better photometric precision. For the MIR, we predominantly use the SpIES and SHELA *Spitzer* IRAC surveys (3.6 μm), since they have better spatial resolution than AllWISE and deeper coverage. However, for archival pointings outside the SpIES or SHELA footprints, we use AllWISE to find infrared counterparts (W1).

2.4. Error Radius for Positional Matching

To determine whether we have identified the same source in two different catalogs, we consider the separation between the two positions. For separations $<1''$ (for SDSS and VHS) and $<2''$ (for IRAC), discrete sources cannot be resolved and are identified as single objects in their respective catalogs. There could be accidental alignments with a random faint source, because they have the largest space density.

For SDSS and VHS, at the faintest magnitudes, the closest pairs lie at $\sim 1\farcs2$, so we are safe in assuming that counterparts within $1''$ are the same object and those with larger separations are distinct objects. For IRAC, the smallest separation between faint sources is $\sim 2\farcs3$, so an error radius of $2''$ is appropriate; that is, IRAC sources should be within $2''$ of the cataloged SDSS or VHS position. Source blending within the error radius can make coordinates inaccurate, as illustrated by Figure 4. Even though SDSS, VHS, and IRAC all identify the same bright counterpart, the IRAC position is less accurate because it is affected by blending with the object above. Therefore, we allow a bigger matching radius for IRAC ($2''$) to account for blending.

As an extra precaution to avoid contamination, we visually inspected all 157 cases (2%) where the separation between the SDSS/VHS and IRAC counterparts is between $1''$ and $2''$ and added comments in our final catalog (Appendix A). Not surprisingly, we found that these cases incorrectly appear extended either due to very crowded fields that cause blending, or due to saturation, or are real extended sources where each band points to a different part of the same object, leading to errors in pinpointing the correct position of the source. For crowded fields, where several objects are too close to each other, we cannot obtain clean photometry, and this will affect the accuracy of the photometric redshifts. Thus, the "nearby_neighbor_sextractor" and the "manual_check" columns in our final catalog are provided to assist the user. The descriptions of all columns in the final catalog are given in Appendix A.

Comparing the positions of all SDSS and VHS counterparts for the *XMM* AO10 and AO13 X-ray sources, we found that 86% are within $1''$ of each other and the median distance between them is $0\farcs19$ (Figure 5). Because the offsets between the SDSS and VHS coordinates are so small, and as both the SDSS and VHS catalogs have sufficiently high resolution to spatially distinguish between sources that are $\sim 1\farcs2$ apart, we conclude that if the counterparts chosen by SDSS and VHS are more than $1''$ apart, they must be two different objects.

Due to the vastly different resolution of AllWISE, those counterparts are not considered unless we do not have a match for a source in any other catalog (66 cases). We do not discard an association completely if it is only detected in one band, because very obscured objects may only be identifiable in the MIR and can potentially be more interesting, e.g., obscured and/or high-redshift AGNs, than bright objects identified in all bands. We provide quality flags and reliability classes to

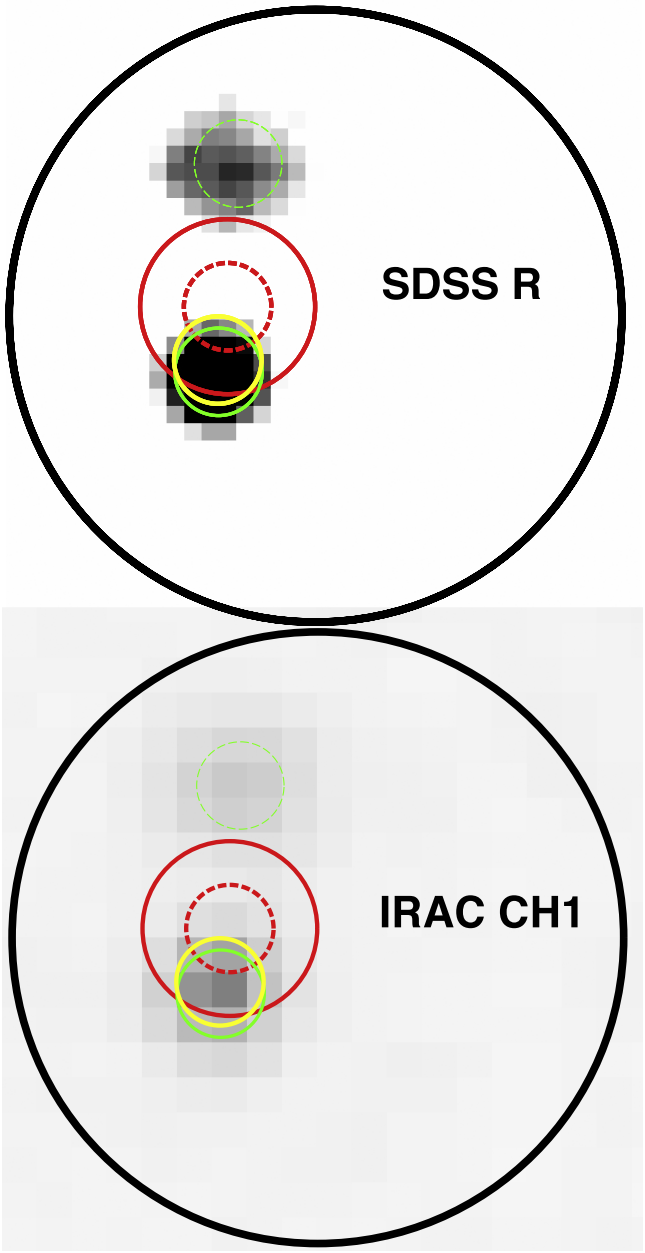

Figure 4. Example of how source positions are affected by nearby sources. Top: SDSS *r*-band image. Bottom: IRAC CH1 image. According to our criteria, the correct counterpart to the X-ray object is the lower source, because the SDSS source position (solid green circle) and VHS source position (yellow circle) agree on this as the most likely counterpart. (The dashed green circle shows another possible SDSS match for this X-ray object but with much lower reliability, so we ignore it.) Note that even though the lower source is brighter in the IRAC image, the IRAC source position (at the center of the red circles) points slightly away, as it is affected by blending with the adjacent faint object. We use two circles of different radii to show the IRAC source position: the dashed red circle is $1''$ in radius, and the solid red circle is $2''$. While comparing source positions between catalogs, if we had used a $1''$ matching radius, we would have incorrectly concluded that IRAC disagrees with SDSS and VHS. Therefore, to account for blending, we allow a $2''$ matching radius for IRAC. To avoid contamination, we visually checked all sources like these where IRAC source position falls between $1''$ and $2''$ from SDSS/VHS and added comments in our final catalog.

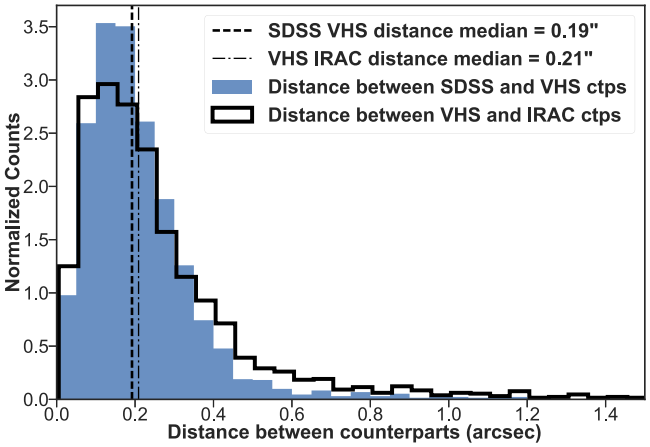

Figure 5. Area-normalized histogram of distances between SDSS *r*-band and VHS *K*-band sources for the *XMM* AO10 and AO13 fields. The median distance between the SDSS and VHS sources is $0\farcs19$, and 86% of the SDSS and VHS counterparts fall within $1''$ of each other. A distance greater than $1''$ indicates that the two counterparts are likely different.

indicate the level of uncertainty in counterpart identification (Section 2.5).

2.5. Resolving Multiple Associations

We find at least one possible counterpart within the search radius of an X-ray source, either in the optical or in the NIR and MIR wavelength, for 97.8% of the Stripe 82X sample. However, not all of the associations are correct, because a fraction of them will be chance associations. We use the likelihood ratio (LR) results from MLE to guide us as to whether a counterpart is reliable. The LR is the probability that the correct counterpart is found within the search radius divided by the probability that the association is a chance coincidence with a background source. We determined a critical threshold (LR_{th}) for each band, below which we assumed that a counterpart is not reliable (these are identified in the master catalog as having a "sub-threshold" reliability class) following the method elaborated in Civano et al. (2012) and Marchesi et al. (2016), which we summarize below.

The LR_{th} is the LR value at which (reliability + completeness)/2 is maximum, where reliability is defined by $R = N_{ID}/N_{LR>L_{th}}$ (ratio of the sum of all the reliabilities of the candidate counterparts and total number of sources above threshold) and completeness $C = N_{ID}/N_X$ (ratio of the sum of reliabilities of all the sources identified as possible counterparts and the total number of X-ray sources; Civano et al. 2012; Marchesi et al. 2016). After determining LR_{th}, we look closely at cases with more than one reliable counterpart identified in any given band (about 10% of the X-ray sources have multiple counterparts above this threshold in at least one band). For each band, we look at the ratio of LR values for the most and the next most reliable counterparts, i.e., $LR_{12} = LR_1/LR_2$. If that ratio is above the median value for all LR_{12} in that band, we assign it a "secure" reliability class. If the ratio falls below the median, we put that source in the "ambiguous" reliability class. Note that this classification is done among counterparts identified within a single band of multiwavelength data for each band on which we ran MLE.

Next, we compare the results of the analysis described above among different bands and find that for 12% of X-ray sources, different bands choose different objects as the most reliable counterpart (Section 2.4). If the two counterparts have different reliability classes (secure, ambiguous, or sub-threshold), we choose the more secure case. If both counterparts have the same reliability class, we choose the one with a higher likelihood ratio. Table 2 lists the reliability class for all counterparts.

Table 2
Summary of Matches within Each Band

Band	Total	$LR > LR_{th}$	Secure	Ambiguous
SDSS[a]	5825 (94%)	5518 (89%)	5358 (87%)	160 (2.6%)
VHS *K*[b]	4253 (69%)	4123 (67%)	3853 (62%)	270 (4.4%)
IRAC CH1[c]	4728 (76%)	4354 (70%)	4102 (66%)	252 (4.1%)

Notes.
[a] FT16 *r* band has LR_{th} of ≈0.6–0.7 and median $LR_{12} \approx 3$–4.
[b] VHS *K* band has LR_{th} of ≈1–1.5 for *XMM* AO10 and AO13 and ≈0.1–0.2 for archival *XMM* and *Chandra*. Median $LR_{12} \approx 1.5$–4.5.
[c] IRAC Ch1 band has LR_{th} of ≈0.8–2.0 and median $LR_{12} \approx 1$–2.5 ($LR_{12} > LR_{th}$ in each field).

As we resolve conflicting associations, we assign quality flags to reflect the confidence with which we identify the correct counterpart.

Quality Flag (QF) 1: For 4524 X-ray sources (73.2%), there is a unique counterpart in at least two bands, and their positions agree, so we consider the identifications unambiguous. For 28 of these sources, the LR is sub-threshold in all bands, but the same counterpart is identified in more than one band; therefore, we consider these unambiguous as well.

Quality Flag 1.5: For 174 sources (2.8%), there are ambiguous counterparts in at least one band, but the other bands help resolve the ambiguity; therefore, these associations are also considered relatively secure.

Quality Flag 2: For 190 sources (3.0%), there are counterparts that disagree, of which one is either sub-threshold or very close to the threshold ($LR < LR_{th} + 2$), while the other is well above the threshold ($LR > LR_{th} + 5$). We choose the latter case regardless of band but flag the association as not quite as secure.

Quality Flag 3: For 416 sources (6.7%), there are different counterparts in multiple bands with comparable LR but different reliability classes (this occurs because LR_{th} and LR_{12} vary between bands). Here we choose the association with the more secure reliability class, assigning it QF 3 and the secondary counterpart QF −1.

Quality Flag 4: For 740 sources (12%), there is a counterpart in only one waveband. Of these, 631 sources have $LR > LR_{th}$, which is considered reliable; 109 sources are below the LR threshold and therefore possibly spurious matches.

Quality Flag 0, −1: A QF 0 indicates that we found no association with that X-ray source in any multiwavelength catalog or that these are sources taken from LM16. There are 137 (2.2%) such sources. QF −1 is an alternate to the association given for QF 3. This means that in the final catalog, one X-ray source can be listed twice, QF 3 being the more secure counterpart and QF −1 being the less secure alternative, according to our MLE analysis.

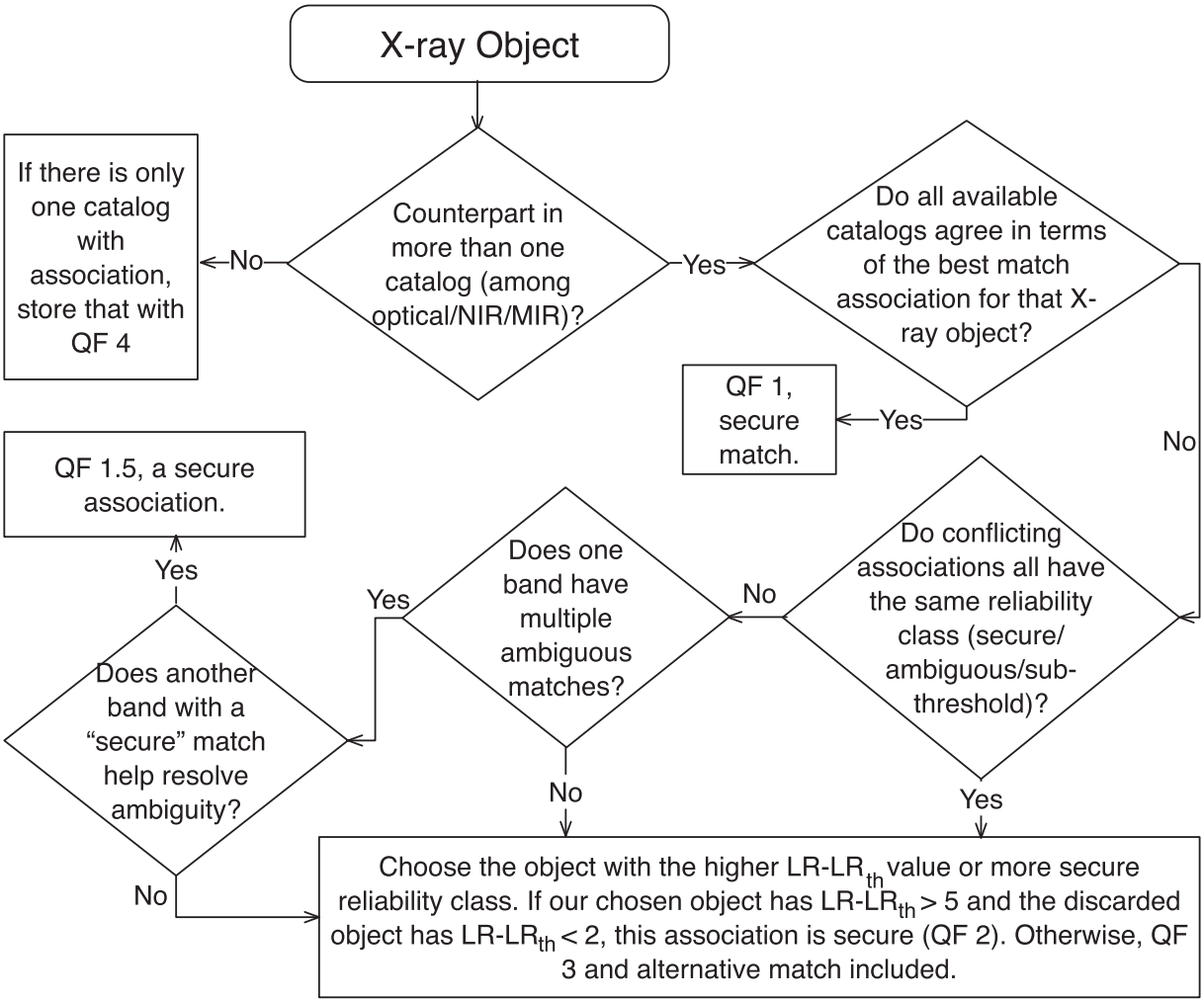

Figure 6. Flow chart showing how we assign counterpart(s) to each X-ray source and how the QF is defined (see Section 2.5). QF values 1, 1.5, and 2 are secure; 3 and 4 are problematic; and −1 refers to the discarded, second-best candidate.

For 173 X-ray sources, there are only matches below threshold (QF 1:28, QF 2:1, QF 3:35, QF 4:109). This totals 6181 X-ray sources to which we assigned a quality flag.

To summarize, of the 6181 unique X-ray sources, 4524 (73%) have unambiguous counterparts in one or more bands (QF 1), 780 (12%) have different counterparts in different bands that we resolve with three levels of confidence (QF 1.5, 2, 3), and 740 (12%) have counterparts in only one band (QF 4). These are considered reliable when they fall above LR_{th} (631 cases), and 137 (2.2%) have no counterparts from our association analysis (QF 0). For 173 (∼3%) sources, there are sub-threshold counterparts (at various QF values). Other than the 29 sub-threshold sources, we take QF 1, 1.5, and 2 sources to be secure.

The flow chart in Figure 6 summarizes the steps in the identification process. We note that some identifications may be improved when deep Subaru HyperSuprimeCam optical imaging becomes available. In our final output catalog (Appendix A), we report the multiwavelength associations and photometry for all objects, along with their reliability classes and quality flags.

2.6. Duplicate X-Ray Observations

There is some overlap between the X-ray observations (between all fields except AO10 and AO13 and AO10 and archival *Chandra*, as shown in Figure 1), resulting in 6181 unique sources and 185 duplicates. The identification of duplicates was done in LM16. We have independently determined the counterparts for all 185 duplicates and found that, even though in most cases duplicate X-ray observations were assigned the same multiwavelength counterpart, in 11 cases (23 observations—10 of these sources have two duplicate observations each, but one source has three different observations), objects identified as the same X-ray source were assigned two different counterparts. This occurs due to slight differences in X-ray coordinates, which in turn changes the surrounding area in which MLE looks for ancillary counterparts.

In order to determine which X-ray source to rely on in case of disagreement of counterparts, we choose the *Chandra* X-ray source over the *XMM* X-ray source due to the high positional accuracy of the former (20 observations of 10 sources). When deciding between duplicate *Chandra* observations (two or three observations of the same source), we choose the source with the lowest positional uncertainty. In the final output catalog, we use a "duplication_flag" to indicate which source we preferred and sources for which counterparts disagreed. The flag is described in Appendix A.

2.7. Summarizing Differences with the LM16 Multiwavelength Catalog

There are some differences between this catalog and LM16 because we use a deeper, updated optical catalog (FT16) and new IRAC catalogs, and because we use a different calculation of the background magnitude distribution used for MLE matching. For 5329 (86%) cases, there is at least one band in which our chosen association agrees with LM16 within 1″. For 40 X-ray sources (0.6%), our chosen counterpart is different from the previous catalog in all bands. There are also 658 new associations (11%) in our catalog due to deeper data. Of these, 507 are above LR_{th} in at least one band. The LM16 catalog purposely did not include any sub-threshold sources, whereas our catalog does (with reliability class marked as sub-threshold) because they are used to resolve conflicting counterparts.

In addition, the LM16 catalog has 20 SDSS counterparts that were not detected in the coadded catalogs that we used. Seven of these sources were not reported in SDSS DR13 (LM16 used DR12), suggesting that they are likely spurious, and we found no counterparts in other bands. We did not include them in our final catalog. Thirteen of the 20 are in the SDSS DR13 catalog because they were detected in one or more bands at one or more epochs. We include these 13 in our final catalog ("Association" field says "LM16"). However, two of these are not detected in any other multiwavelength catalogs (VHS, IRAC, AllWISE, coadded SDSS) and so should be considered with caution.

Another five have detections in only one of those wavebands, which is better but also requires caution. Finally, five have detections in five or more wavebands and have coadded SDSS data as well, but after the offset correction that we applied, they fall outside the X-ray error radius (5″–7″), so our MLE analysis ignored these possible associations. There is one source from LM16 for which we get two bands of data, in the VHS J and H bands, but as we do not run MLE in these bands, we miss this association. We annotate these 13 objects with the appropriate "manual_check" in our final catalog.

2.8. SED Construction

Before constructing broadband SEDs, we identify NIR counterparts in the UKIDSS catalog (Lawrence et al. 2007) and ultraviolet (UV) counterparts in the *GALEX* catalog (Martin et al. 2005) using nearest-neighbor matching. These catalogs are not used for association analysis, but once we have identified a counterpart with an appropriate QF, nearest-neighbor matching with an error radius is sufficient to identify that counterpart in ancillary catalogs. Table 3 shows the error radius allowed between different ancillary catalogs to construct the final multiwavelength catalog (Appendix A). For the nearest-neighbor match, the counterpart coordinate comes from the catalog with the most accurate astrometry (as in Section 2.5); for example, if the SDSS and IRAC counterparts for an X-ray source agree, we choose the SDSS coordinates because of their better positional accuracy.

Like VHS, UKIDSS provides broadband data in the J, H, and K filters but is shallower (and thus with larger photometric errors; see Figure 7), with a 5σ K_{AB} depth of 20.1 mag. We still include UKIDSS when constructing SEDs (but do not use it in the analysis in Sections 2.3–2.5) to check if having additional NIR data leads to more robust photometric redshifts; we discuss the results in Section 3.5. Roughly 58.7% of the X-ray sources have UKIDSS counterparts. Because the *GALEX* survey of Stripe 82 is relatively shallow, we find UV counterparts for only 20% of the X-ray sources.

We correct the UV, optical, and NIR data for extinction using the Galactic extinction values from SDSS DR13 (SDSS Collaboration et al. 2016) and color excess from VHS (McMahon et al. 2013). The corrected magnitudes can then be compared to template SEDs. (The transformation of template SEDs to the observed photometric system is discussed in Section 4.1 of S09.)

To summarize, the SEDs consist of far- and near-ultraviolet (FUV and NUV, respectively) from *GALEX*; u, g, r, i, and z from SDSS; J, H, and K from VHS/UKIDSS; CH1 and CH2 from IRAC; and W1 and W2 from AllWISE. We also provide AllWISE W3 and W4 magnitudes in our final catalog, but it is not used for SED construction. The bands used for SED fitting are discussed in Section 3.5.

Table 3
Search Radius Allowed for Nearest-neighbor Matches between Ancillary Catalogs

Catalog	SDSS and VHS	IRAC
SDSS DR12 redshifts	1.″0	2.″0
GALEX	2.″0	2.″0
SDSS (FT16)	1.″0	2.″0
SDSS (J14)	1.″0	2.″0
VHS	1.″0	2.″0
UKIDSS	1.″0	2.″0
SpIES	2.″0	1.″0
SHELA	2.″0	1.″0
AllWISE	1.″0	1.″0

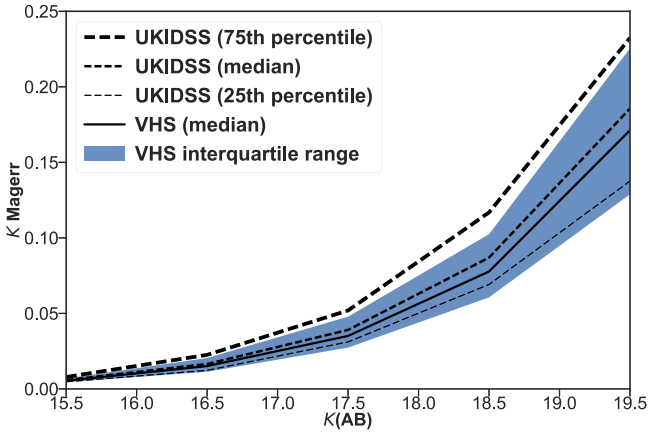

Figure 7. VHS and UKIDSS K-band magnitude errors plotted against K-band magnitude. The VHS magnitude errors are slightly smaller than the UKIDSS magnitude errors, and VHS is slightly deeper, so we only use VHS for MLE matching. However, we add the UKIDSS data after finding associations and use it to construct SEDs.

3. Photometric Redshifts

We present photometric redshifts for a total of 96.4% (5961) of the sources of Stripe 82X; missing are the 2.2% (137) without counterparts in other wavebands and the 1.4% (83) with data in only one or two bands, which is insufficient for template fitting. In this section, we discuss the procedure to calculate photometric redshifts.

3.1. Method of Fitting SEDs

We computed photometric redshift via the SED fitting technique using the code LePhare (Arnouts et al. 1999; Ilbert et al. 2006), which has been extensively used and tested both for normal galaxies and for AGNs. LePhare can accommodate user-specified SED templates, extinction law(s), and extinction value(s). In addition, it allows the use of luminosity priors to reject unlikely redshifts. Finally, LePhare corrects for intergalactic absorption, an important effect for high-redshift sources.

Since the mix of active nucleus and host galaxy can be different in every object, the fitting process is more complicated than for normal, inactive galaxies. This added complexity manifests as degeneracy in the results, as small parameter shifts cause more than one template to be a good fit to the photometric SED.

In order to break this degeneracy, we use secondary information to limit the parameter space of the redshift solution. The full-width at half maximum (FWHM) of sources in ground-based optical images, for example, can tell us whether the source is at low redshift: sources classified as "extended" in ground-based images cannot be at redshift $z > 1$, and their SEDs will have a large host galaxy contribution.

In contrast, a point-like source will either have a high redshift or be a star or a quasar, and these considerations translate into templates and luminosity priors that increase the accuracy of the derived photometric redshifts. Accordingly, we treat point-like and extended sources differently, as shown in S09.

Photometric catalogs usually provide morphology information, or typical FWHMs of stars/point-like objects in different bands. We rely on ground-based morphology provided by FT16, J14, and McMahon et al. (2013). The exact procedure for the classification into these two subsamples is discussed in Section 3.3. Note that the use of morphological classification done on lower-resolution, ground-based images rather than on *Hubble Space Telescope* (*HST*) images, as in S09, will affect our results, as we explain in Section 3.3.

Photometric redshifts are calibrated using the objects that have spectra (see Section 3.6 for more details). We start by selecting a limited set of SED templates, large enough to represent the full sample yet small enough to avoid degeneracy in χ^2 fitting. We do this separately for the two subsamples (extended and point-like; described in Section 3.3). Using trial and error, we try to achieve photometric redshifts that have small normalized median absolute deviations,

$$\sigma_{\rm nmad} = 1.48 \times {\rm median}(|(z_{\rm spec} - z_{\rm phot})/(1 + z_{\rm spec})|), \quad (1)$$

and a low outlier fraction (η), where outliers are sources that have

$$|(z_{\rm spec} - z_{\rm phot})/(1 + z_{\rm spec})| > 0.15 \quad (2)$$

with respect to the spectroscopic redshifts.

The process of choosing correct luminosity priors, extinction laws, and color excesses was very similar to that of S09. We used the same extinction law (Prevot et al. 1984) and values for the extinction $E(B - V) = (0, 0.1, 0.2\text{–}0.5)$ and luminosity priors as in S09, as these settings produced the most reliable results by trial and error. The luminosity priors used for each subset are the same as those used in S09: an absolute magnitude range of -24 mag $< M_g < -8$ mag for extended and -30 mag $< M_g < -20$ mag for (optically) point-like objects. We fit the SEDs across a redshift range of 0.03–7.0 in steps of 0.01.

The best-fit photometric redshift is based on the minimum χ^2 of the fit. Two example SED fits are shown in Figure 8. In the first case, the photometric redshift solution is unique, while in the second case, there are two possible solutions at different redshifts, obtained with different templates. In addition to the photometric redshift ($z_{\rm phot}$) for each source, LePhare provides the redshift probability distribution function, $P(z)$. We define a quality metric, PDZ, as the probability that the true redshift is within $\pm 0.1(1 + z_{\rm phot})$ of $z_{\rm phot}$:

$${\rm PDZ} = 100 \times \frac{\int_{z_{\rm phot}-0.1(1+z_{\rm phot})}^{z_{\rm phot}+0.1(1+z_{\rm phot})} P(z)dz}{\int_0^\infty P(z)dz}, \quad (3)$$

where

$$P(z) = \frac{\exp[-\frac{\chi^2\,{\rm min}(z)}{2}]}{\exp[-\frac{\chi^2\,{\rm min}({\rm zbest})}{2}]}. \quad (4)$$

In LePhare, we set very low values of MIN_THRES (0.005) and DZ_WIN (0.025; see LePhare manual) so that secondary peaks in the redshift probability distributions could be identified. Our output catalogs and SED fit plots report these secondary redshifts, as well as the $\chi^2_{\rm sec}$ and ${\rm PDZ}_{\rm sec}$, as shown in Figure 8 (top right and bottom right panels).

The selection of template library and extinction laws was done using all the spectroscopy from SDSS DR13 and DR12. Afterward, we added in more redshifts from DR12, DR10, and additional surveys listed in Section 1 (~20% of the whole spectroscopic sample). Therefore, we were treating the initial 80% as our training set and the 20% we added in later as a test set. The two subsets (initial data and added data) have similar outlier fractions and overall accuracy. After this paper was submitted, SDSS DR14 was released (Abolfathi et al. 2017). We present the results for this new spectroscopic sample in Section 4.

3.2. Representative Set of Templates

As discussed in Section 2.1, our survey has a larger volume and is shallower than fields for which photometric redshifts have previously been calculated. The difference between populations in this work and previous deeper photometric redshift works is summarized in Table 4.

In particular, Stripe 82X tends to have more high-luminosity quasars and AGN-dominated emission, as evidenced by the higher fraction of high soft flux (flux in 0.5–2 keV band) sources. As a result, we could not use the template set optimized for the deeper fields; instead, we began with a large selection of templates from which we selected a smaller set best suited to Stripe 82X. In Appendix B, we describe the process for selecting suitable templates for SED fitting, and we give an example of how we rejected a particular template.

We started with templates used by Ilbert et al. (2009), S09, S11, and Hsu et al. (2014) for galaxies and AGNs in deep, pencil-beam surveys (CDFS, ECDFS, *Chandra*-COSMOS, and *XMM*-COSMOS). Hsu et al. (2014) constructed hybrids combining AGN templates with semi-empirical star-forming galaxy templates from Noll et al. (2009). We tested each of these libraries on our spectroscopic sample, noted which templates were frequently providing us with the best fits and

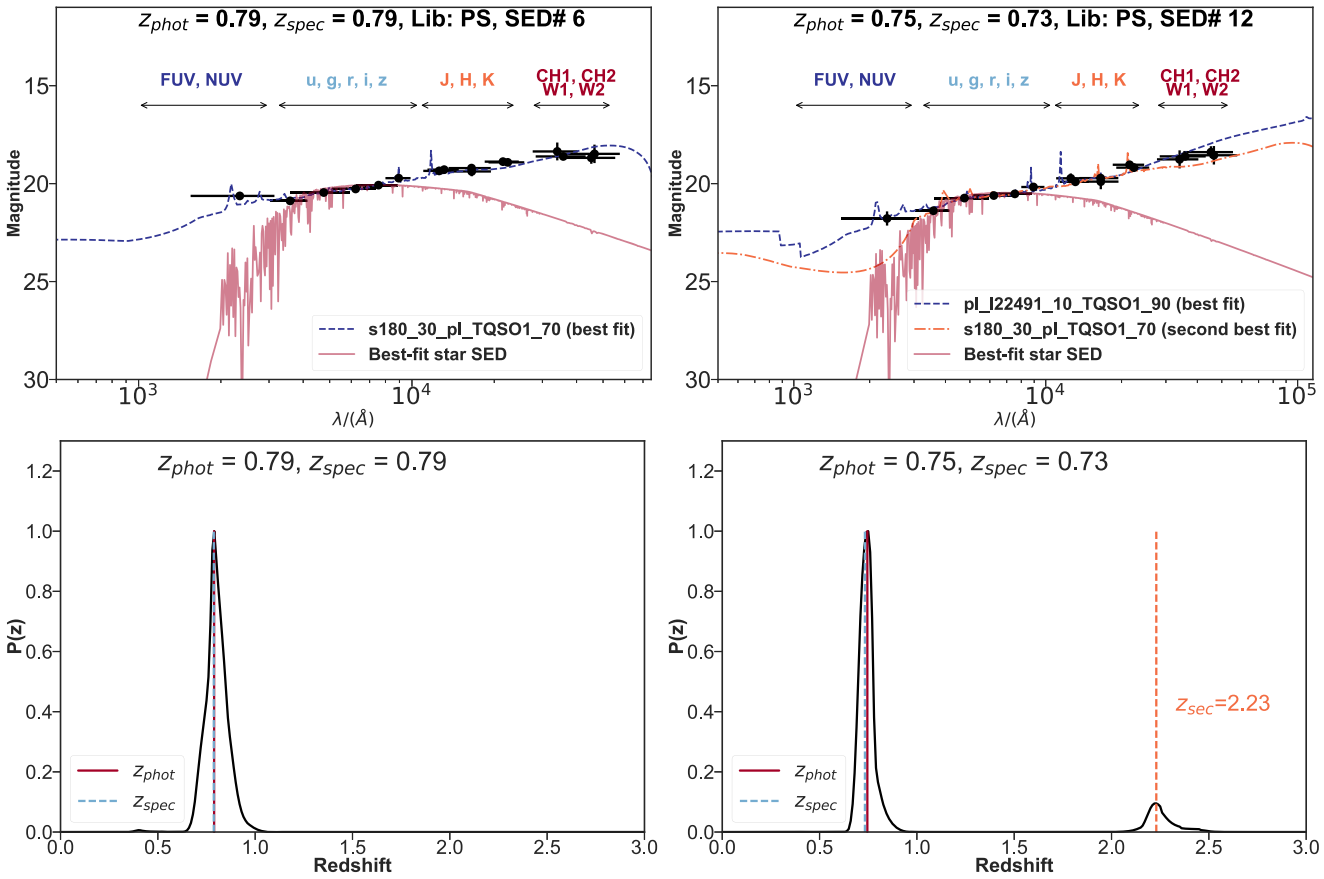

Figure 8. Top panels: best-fit templates (blue dashed lines) for observed SEDs (black points) of two Stripe 82X AGNs, one with a well-defined redshift and a similar one that also has a secondary redshift. Bottom panels: probability function of photometric redshifts for these objects. Top left: point-like AGN (r-band FWHM $<1\farcs1$) fitted with a template that is 30% spiral galaxy and 70% Type 1 quasar (from the point-source library; see Table 5); also shown is the best-fit stellar template (faint solid red line). Top right: point-like AGN fitted with 10% I22491 starburst galaxy plus 90% type 1 quasar (blue dashed line, best fit) or 30% spiral galaxy plus 70% Type 1 quasar (orange dash-dotted line, second-best fit). For the bottom panels, the peak probability value indicates the redshift for the best-fit template, and, when present, a secondary peak indicates a second template that fits the SED well at a secondary photometric redshift (bottom right panel).

fewest outliers, and, by trial and error, selected a small set of templates that minimized the outlier fraction and $\sigma_{\rm nmad}$.

In general, spectroscopy is only possible for brighter objects (see Figure 9), and photometric redshifts are needed for the faintest sources in a sample. So there is always a possibility that the relatively bright population on which the photometric redshifts are calibrated is systematically different from the faint sources. We took this into account by including templates that would fit the AGN-dominated sources (mostly Type 1 or starburst spectra) and templates that would fit fainter objects not represented in the spectroscopic sample (Type 2 templates). Newly released SDSS DR14 (Abolfathi et al. 2017) spectra made it possible to test our accuracy using a blind sample of objects fainter than our training set. The results of this test are discussed in Section 4.

The final list of templates is given in Table 5. As we mentioned in Section 2.1, our template library has also been used to calculate photometric redshifts for *XMM*-XXL (Georgakakis et al. 2017), providing a better accuracy than the original library defined in S09. Thus, we believe this library would be more appropriate for the *eROSITA* all-sky survey, which has a depth similar to that of Stripe 82X and *XMM*-XXL (see bottom panel of Figure 2). This library should also be considered when computing the $z_{\rm phot}$ of AGNs in wide surveys, such as the Dark Energy Survey (DES), Euclid, and, more importantly, LSST.

3.3. Classification as Point-like or Extended Optical/IR Sources

S09, S11 demonstrated how morphological information, combined with a prior in absolute magnitude, improves the reliability of photometric redshifts for AGNs. Ideally, as in COSMOS and other deep pencil-beam surveys, the morphological information comes from *HST* without seeing effects deforming the images. For Stripe 82X, we get morphological information from ground-based SDSS images. Besides the lower spatial resolution of the images, we have to deal with the fact that when the seeing is poor, the stars used for defining the PSF are also smeared. This means sources that ought to be classified as extended are wrongly classified as point-like. A quantification of this effect was given in Hsu et al. (2014).

As mentioned in Section 2, FT16 created deep stacked images from which low-quality data were removed, improving on the overall photometry and morphological classification. We determined that the FT16 classification as point-like or extended is the most reliable compared to other available morphological information because it gives the smallest number of outliers in the comparison of photometric and spectroscopic redshifts. Using the J14 morphological

Table 4
Population Type Comparison between Different Fields[a]

Field	Source Count[b]	Extended Source Count[c]	Point-like Source Count[d]	$F_{0.5-2\,\mathrm{keV}} > 1e^{-14}$ erg cm^{-2} s^{-1}
S82X	6044[e]	2486 (41%)	3289 (54%)	2304 (38%)
Lockman Hole (Fotopoulou et al. 2012)	388	134 (34.5%)[f]	140 (36%)	19 (5%)
CDFS (Hsu et al. 2014)	744	591 (79%)	153 (21%)	7 (1%)
ECDFS (Hsu et al. 2014)	1207	974 (81%)	233 (19%)	19 (2%)
Chandra-COSMOS (Marchesi et al. 2016)	4016[g]	2023 (50%)	1726 (43%)	221 (5.5%)
XMM-COSMOS (S09)	1542	464 (30%)	1032 (67%)	179 (11.6%)

Notes.
[a] More details about each of these fields is given in Table 8. This table does not include fields for which z_{phot} were only calculated for point-like sources.
[b] Sources that had associations or were categorized as extended and point-like sources.
[c] Extended sources tend to be nearby and galaxy-dominated.
[d] Point-like sources tend to be AGN-dominated and variable.
[e] 6044 out of 6181 have associations, and 269 could not be categorized as point-like or extended.
[f] 103 are too faint to resolve, and 12 are blended with nearby sources.
[g] Not all objects could be categorized as point-like or extended due to lack of optical counterpart.

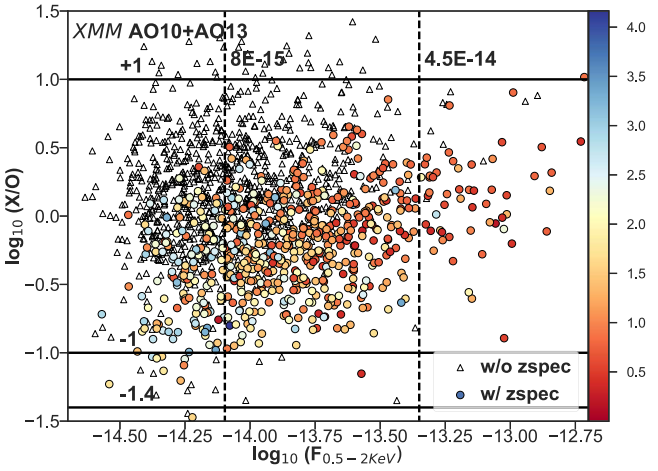

Figure 9. Log of the X-ray-to-optical flux ratio vs. the log of the soft X-ray flux (0.5–2 keV band) of all point-like objects in *XMM* AO10 and AO13. The ratio X/O is based on the soft X-ray flux and the SDSS i-band flux. The spectroscopic sample is color-coded by redshift. This plot shows that the spectroscopic sample tends to be brighter than the nonspectroscopic sample, although they span the same range in flux and redshift.

information, our results had around 25% outliers, whereas using FT16 helped us reduce that to around 14%.

We summarize the classification process in Figure 10. When FT16 classification was not available (18% of objects), we used the information from J14, ideally in the r band (for 6% of the objects); failing that, we used the information from the i, z, g, and u bands, in that order (4%). If no optical information was available, we used the NIR morphology from VHS data (2%); specifically, if PGAL >0.5 (McMahon et al. 2013), we consider the object extended; otherwise, we consider it point-like.

Objects that are not extended in the SDSS or VHS data are grouped with the point-like objects but flagged as uncertain. In the end, 40% (2486) of the Stripe 82 X-ray sources are clearly extended, 53% (3289) are clearly point-like, and 5% (269) are tentatively point-like but flagged uncertain. The remaining 2% (137) do not have a multiwavelength counterpart.

We indicate the final morphology assigned to a source using the "classification" column in the final output table, as described in Appendix A. Once objects have been classified as point-like or extended, we apply a different set of templates

Table 5
Library of Templates[a] for Point-like[b] and Extended Sources[c]

Point-like SED Templates	Extended SED Templates
1: I22491_80_pl_TQSO1_20	26: M82
2: I22491_90_pl_TQSO1_10	27: I22491_10_pl_TQSO1_90
3: pl_QSOH_template_norm	28: I22491_20_pl_TQSO1_80
4: pl_TQSO1_template_norm	29: I22491_50_pl_TQSO1_50
5: s250_10_pl_TQSO1_90	30: I22491_60_pl_TQSO1_40
6: s180_30_pl_TQSO1_70	31: I22491_80_pl_TQSO1_20
7: s800_40_pl_TQSO1_60	32: I22491
8: fdf4_40_pl_TQSO1_60	33: Ell2
9: s800_20_pl_TQSO1_80	34: Ell5
10: I22491_30_pl_TQSO1_70	35: Ell13
11: I22491_20_pl_TQSO1_80	36: S0
12: I22491_10_pl_TQSO1_90	37: Sa
13: I22491_50_pl_TQSO1_50	38: Sb
14: Spi4	39: Sc
15: Sey2	40: Sdm
16: S0_10_QSO2_90	…
17: S0_20_QSO2_80	…
18: S0_30_QSO2_70	…
19: S0_40_QSO2_60	…
20: S0_50_QSO2_50	…
21: S0_60_QSO2_40	…
22: S0_70_QSO2_30	…
23: S0_80_QSO2_20	…
24: S0_90_QSO2_10	…
25: Mrk231	

Notes.
[a] S150, S180, S800, fdf4, M82, Mrk231, and I22491 are starburst galaxies with different levels of star formation. TQSO1 and QSO2 are type 1 and type 2 AGN templates. QSOH is a high-luminosity quasar. Sey2 is a Seyfert 2 template. Spi4, S0, Sa, and Sb are spiral galaxies, and Ell2, Ell5, and Ell13 are ellipticals. I22491_80_pl_TQSO1_20 is an 80% I22491 and 20% QSO1 template. These templates are described in detail in Ilbert et al. (2009), S09, and Hsu et al. (2014).
[b] Point-source templates include hybrids of galaxy, quasar, and AGN spectra.
[c] Extended-source templates include elliptical, spiral, and starburst galaxies and starburst-QSO hybrid spectra.

(summarized in Table 5) and priors to these two morphological classes to calculate photometric redshifts.

For 1156 objects with saturated photometry or bright nearby neighbors (∼16%), we calculate photometric redshifts but flag them as uncertain. We discuss the accuracy and outlier

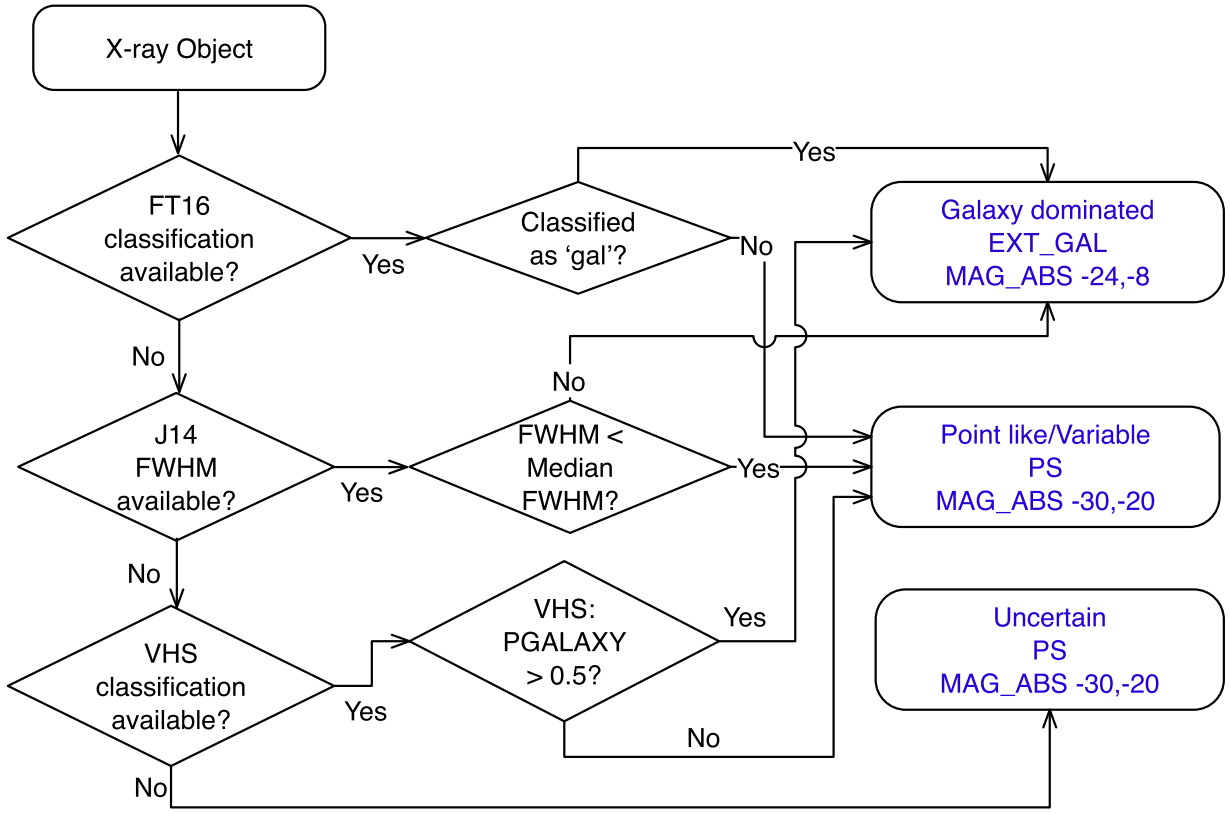

Figure 10. Procedure used to classify AGNs as point-like or extended based on optical and NIR morphology. Based on this classification, different luminosity priors and template libraries are applied to these objects to calculate photometric redshifts.

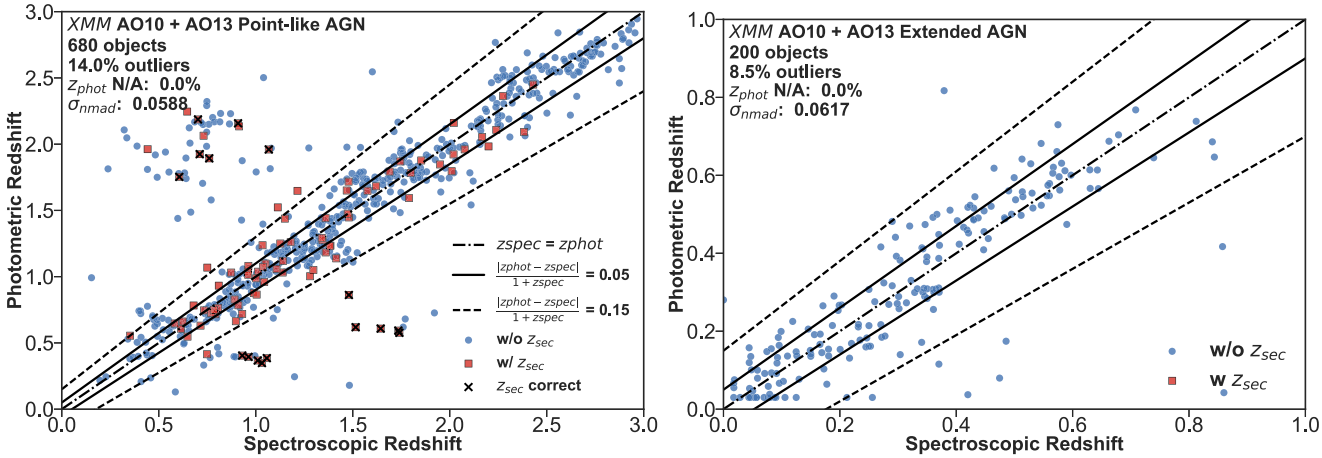

Figure 11. Spectroscopic vs. photometric redshift for point-like (left) and extended (right) sources in the uniform *XMM-Newton* fields. The results in the other fields are very similar, as can be seen in Table 7. Black crosses indicate cases where the primary redshift is incorrect and the secondary redshift is correct (i.e., it lies within the dashed black lines). The quantity "$z_{\rm phot}$ N/A" reports the percentage of sources for which we are unable to calculate photometric redshifts altogether due to data in very few bands or not having an appropriate SED template in our template library.

fractions of objects with and without bright nearby neighbors separately, as the photometry of the former is not reliable.

The comparison of photometric and spectroscopic redshifts for point-like and extended AGNs in the *XMM* AO10 and AO13 samples (to differentiate from the *XMM* archival sample) is shown in Figure 11. A census of all of the sources is given in Table 6.

3.4. Photometric Inhomogeneities among Wavebands

The success of photometric redshifts, especially for AGNs, is determined to a large extent by the homogeneity of the optical and infrared photometry from different surveys. While photometry in pencil-beam areas is relatively homogeneous—e.g., CANDELS fields (Hsu et al. 2014), the entire COSMOS (S09, S11), and AEGIS surveys (Nandra et al. 2015)—the situation is worse for wide-field areas.

In particular, Stripe 82X has NIR photometry reported for different apertures in images of different resolution, i.e., sampling different amounts of the host galaxies. SpIES and SHELA provide aperture and SEXTRACTOR (Bertin & Arnouts 1996) AUTO fluxes (a Kron-like flux) for *Spitzer* IRAC sources, while the VHS catalog reports Kron, PSF, and

Table 6
Summary of Available Photometric Redshifts by Subsample for the 6181 Stripe 82X Sources[a]

Type	*XMM* AO10 + AO13	Archival *XMM*	*Chandra*	Total
Total	3613	1607	1146	6366
After removing duplicates	3541	1496	1144	6181
Objects with associations	3516 (99%)	1450 (97%)	1061 (93%)	6027 (98%)
All point-like	1976 (56%)	757 (51%)	546 (48%)	3279 (53%)
With z_{spec}	793 (23%)	292 (20%)	246 (22%)	1331 (22%)
All extended	1404 (40%)	641 (43%)	434 (38%)	2479 (40%)
With z_{spec}	288 (8%)	138 (9%)	108 (9%)	534 (9%)
Cannot classify[b]	136 (4%)	52 (3%)	81 (7%)	269 (5%)
No associations	25 (1%)	46 (3%)	83 (7%)	154 (2%)
Reporting z_{phot} for[c]	3501 (100%)	1418 (95%)	1025 (91%)	5944 (96%)

Notes.
[a] All percentages relative to the total number of nonduplicate sources and rounded to the nearest integer.
[b] There are multiwavelength associations in at least one band for these sources, but we do not have enough SDSS or VHS information for proper classification. We calculate photometric redshifts for these sources assuming they are point-like.
[c] Number of X-ray sources for which we are reporting photometric redshifts. Photometric redshifts calculated with less than two bands of data should not be considered reliable. To assist the user, we provide the "num_filt" column in our final catalog with the number of bands of data available for a source.

Petrosian magnitudes. The photometry reported in *GALEX* also provides AUTO magnitude, whereas the AllWISE catalog provides a total flux (though this is affected by source blending). Optical photometry is available for different aperture sizes, as well as Petrosian and AUTO magnitude.

Under these circumstances, computing and correcting for systematic zero-point effects (e.g., Ilbert et al. 2009; Hsu et al. 2014; S09) is at best difficult and at minimum unreliable. For this reason, we came up with a compromise approach: instead of applying systematic shifts, we tested different types of photometry in order to find the combination that provides the highest accuracy and the smallest fraction of outliers.

Accordingly, after some experimentation, we decided to use AUTO magnitudes (where available) for both extended and point-like sources. Only for the NIR, we decided on a 2.″8 radius aperture magnitude for point-like sources and 5.″7 radius aperture magnitude for extended sources after testing several aperture sizes for each sample. For AllWISE, we provide *mpro* magnitudes in all four bands, although we only use *w*1*mpro* and *w*2*mpro* to construct SEDs.

3.5. Improving Accuracy Using UKIDSS and AllWISE

In Section 2.8, we noted that we tried including UKIDSS and AllWISE photometry in the fitted SEDs, even though VHS/IRAC bands cover the same wavebands with slightly better accuracy, because we wanted to determine whether having additional bands of data over the same range of wavelengths led to better photometric redshifts. We found that excluding UKIDSS and AllWISE in cases where we have VHS/IRAC marginally improves the results by lowering outliers by ∼1% in the overall sample and leads to fewer cases where we are completely unable to compute photometric redshifts.

Therefore, we do not use UKIDSS photometry if we have VHS data available. Similarly, we ignore AllWISE data if we have IRAC data available. Other than these exceptions, we use all available bands from FUV to W2/CH2 for SED fitting. We report AllWISE W3 and W4 magnitudes in the final catalog but do not use them for z_{phot} calculation. Note that we do use UKIDSS and/or AllWISE bands to compute photometric redshifts for objects that do not have VHS/IRAC data.

3.6. Accuracy of Spectroscopic Redshifts

The accuracy of photometric redshifts is based on a sample of secure spectroscopic redshifts. In practice, the fitting procedure, classifications, templates—all the aspects of determining photometric redshifts—are adjusted to produce the most accurate results with respect to the spectroscopic sample. Therefore, to ensure the most accurate results, we excluded any spectroscopic redshifts flagged as uncertain.

SDSS DR12Q (Pâris et al. 2017) presents quasar redshifts that have been visually inspected and are therefore reliable. For cases where we do not find any redshifts from DR12Q, we look for redshifts in SDSS DR13 (SDSS Collaboration et al. 2016). For DR13, no public visual inspection information is yet available, and the pipeline sometimes returns multiple redshifts for the same object. This occurs because the reliability of a redshift is dependent upon the signal-to-noise ratio of the spectrum (discussed in detail in Menzel et al. 2016) and the nature of the source.

We found that for 300 cases, the same object was associated with more than one redshift in DR13, with no warning flag (zwarning = 0). Among these, 289 sources have multiple redshifts that agree down to two decimal places. A difference on the third decimal place corresponds to a velocity of about 1000 km s^{-1}, which is below our photometric redshift sensitivity of 0.01 (due to a limited number of bands). For these cases, we select the redshift with the lowest error. For the 11 cases where the difference is significant or two different object types (AGN/star) are identified by two different spectra, we proceeded to a visual inspection and determined the correct redshift. We made use of Dwelly et al. (2017) to visually inspect all DR13 spectra reported in this work.

SDSS DR10, DR12Q, and DR13 provide redshifts for 1577 cases, and additional spectroscopy (sources listed in output table and LM16) provides redshifts for another 288 sources; the latter have also all been visually inspected.

4. Results and Discussion

We calculated photometric redshifts following the methods explained in Section 3 for 96% of the Stripe 82X X-ray sources and achieved an overall accuracy (σ_{nmad}) of 0.06 and an outlier fraction (η) of 13.69%. The σ_{nmad} and η of each subset of the data are given in Table 7. These results do not take into account objects with bright nearby neighbors. As photometry for such cases is less reliable due to contamination, their η and σ_{nmad} are calculated separately. There are 352 spectroscopic objects with bright nearby neighbors, and this sample has $\eta = 19.32\%$ and $\sigma_{nmad} = 0.0882$.

The population that we are probing is brighter in the X-ray than populations in fields such as CDFS, so a typical AGN in our population is composed of a power law plus emission lines.

Table 7
Photometric Redshift Outlier Fractions and Accuracy for All Three Fields[a]

Object Type		*XMM* AO10 + AO13	Archival *XMM*	*Chandra*	Total
Point-like AGN	Total number with z_{spec}	797	292	246	1335[b]
	W/o bright nearby neighbor	680	247	208	1135
	Outlier	14.0%	14.6%	19.7%	15.18%
	σ_{nmad}	0.0588	0.0605	0.0573	0.0589
Extended	Total number with z_{spec}	288	139	109	536
	W/o bright nearby neighbor	200	94	79	373
	Outlier	8.5%	9.6%	10.3%	9.14%
	σ_{nmad}	0.0617	0.0618	0.0733	0.064
Overall	Total number with z_{spec}	1081	430	354	1865
	W/o bright nearby neighbor	878	341	286	1505
	Outlier	12.76%	13.20%	17.13%	13.69%
	σ_{nmad}	0.0595	0.0609	0.0617	0.0602

Note.
[a] The outlier percentage and accuracy values reported here only apply to objects without SDSS photometry flags indicating contamination due to bright nearby neighbors.
[b] This number includes stars, which we eliminate using the method described in Section 4.5.

Objects that have a significant galaxy component tend to have emission lines, and, with narrowband or intermediate-band photometry, these lines would be identifiable, making their photometric redshifts more accurate. However, with broadband photometry, the correct model is harder to pinpoint, which leads to a higher η and σ_{nmad}.

Similar to previous AGN photometric redshift works (S09; Hsu et al. 2014), we find more accurate redshifts for point-like objects but with a higher percentage of outliers than for extended objects. As in Hsu et al. (2014), most of the outliers in the point-like samples have an overestimated photometric redshift. The problem is related to the wrong morphological classification, which is done in this work using ground-based images. Figure 11 shows a plot of z_{phot} against z_{spec}. The plot on the left is for point-like objects, where a fraction (18%) of the outliers have secondary photometric redshifts that are very close to the spectroscopic redshifts (both primary and secondary photometric redshifts are given in Appendix A).

The redshift distribution for our objects is given in Figure 12. Spectroscopic and photometric redshifts lie within the same range, but the photometric redshift distribution shows an overdensity at $z \sim 0.75$ (between 0.5 and 1). We tested whether this peak could be due to a systematic effect in our computation process. In particular, we tested the impact of switching priors and libraries on the two subsamples (extended and point-like).

We found that the extended sources work equally well with the point-like sample's priors and libraries, but not vice versa. This is because the point-like sources' library includes AGN-galaxy hybrids that also apply to extended objects. Additionally, extended sources host an AGN with absolute magnitudes that are within the range allowed by the point-like sample's prior.[18] Point-like sources are not fitted well by the extended sample's templates. The high absolute magnitude priors for extended sources force LePhare to assign the lowest possible redshift ($z \sim 0.03$) to a significant fraction (25%) of the point-like objects whose photometric redshifts lie in the overdensity region. Thus, the overdensity is not due to systematic effects from the SED fitting.

[18] Note that there cannot be many extended nonactive galaxies in our sample because the template fits would have failed.

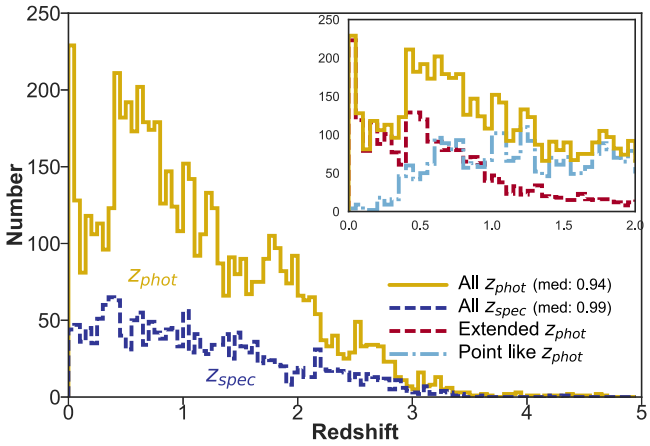

Figure 12. Best-fit photometric (*gold*) and spectroscopic (*blue*) redshift distributions for all 5716 sources with good photometry. The overdensity at $z \sim 0.75$ in the distribution of photometric redshifts is not echoed in the spectroscopic distribution, suggesting that fainter sources are more clustered at $z \sim 0.7$ than bright sources. The inset shows that the populations of extended and point sources cross at this approximate redshift; we checked that point sources were not mistakenly identified as extended (see the text for details).

Overdensities at redshift ~0.8 are a common feature in all photometric redshift distributions for deep surveys (e.g., Barger et al. 2003; Gilli 2004; Szokoly et al. 2004), and a similar overdensity has been seen for star-forming galaxies and emission-line galaxies (Sobral et al. 2013; Favole et al. 2016; Iovino et al. 2016).

In the context of the LCDM cosmological model, characterized by the observationally determined values for cosmological parameters like Λ and H_0, z~0.8 is the redshift at which the universe switches from being matter-dominated to dark energy–dominated. At this epoch, the Hubble distance (which is a function of cosmological parameters) changes slope (Aubourg et al. 2015).

Another potential explanation is that the competition between the increase in accessible volume with redshift and the decreasing number of detectable objects crosses over at this cosmic epoch, leaving the imprint of a peak in the redshift distribution. This makes sense if the objects with spectroscopic redshifts are luminous enough that none have been excluded by

Table 8
Comparison of Photometric Redshifts for X-Ray Surveys with Different Depths (of X-Ray and Multiwavelength Data) and Number of Photometric Bands

Field	Ref.	Area	Number of Sources	Mean Exp Time	Soft Flux Limit	Bandwidth	Accuracy	Outliers
		(deg^2)		(ks)	($F_{0.5-2\,keV}$)	N/I/B[a]	(σ_{nmad})	η (%)
S82 Archival *Chandra*		6	1146	5.7–71.2	8×10^{-16}	B	0.0627	17.1
S82 Archival *XMM*		7.4	1607	17–65	7×10^{-17}	B	0.0609	13.2
S82 *XMM* AO10+AO13		20.2	3613	4–8	2×10^{-15}	B	0.0595	12.8
Lockman Hole	Fotopoulou et al. (2012)	0.20	388[b]	185	1.9×10^{-16}	B	0.069	18.3
CDFS	Hsu et al. (2014)	0.13	740	2000	9.1×10^{-18}	I	0.014	6.73
ECDFS	Hsu et al. (2014)	0.3	762	250	1.1×10^{-16}	I	0.016	10.14
AEGIS-XD	Nandra et al. (2015)[c]	0.29	1325	200	5.3×10^{-17}	N/B	0.022	2.8
Chandra-COSMOS	Marchesi et al. (2016)	0.90	4016	200	1.9×10^{-16}	N/I/B	0.015	6
XMM-COSMOS	S09	2.13	1887	60	1.7×10^{-15}	N/I/B	0.015	6.3[d]

Notes.
[a] N, I, and B stand for narrowband, intermediate-band, and broadband, respectively.
[b] For X-ray-detected sources (3.9σ significance), which are more similar to our sample.
[c] This paper only includes photometric redshifts for point sources, but we report the total number of sources in this table.
[d] For the QSOV sample.

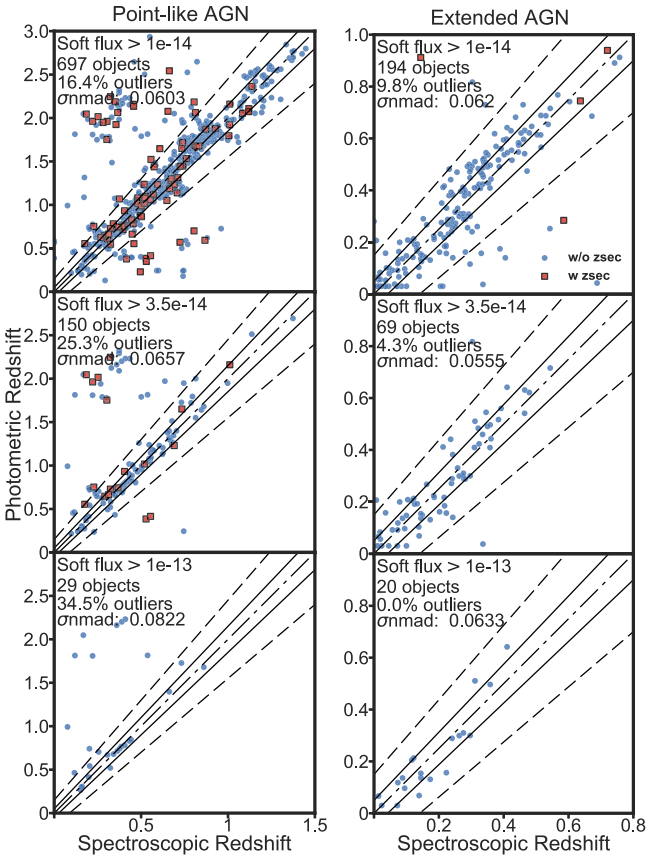

Figure 13. Difference in accuracy and outlier numbers for spectroscopic samples selected by limits on soft flux (0.5–2 keV). These values are also summarized in Table 9.

the flux limit. Indeed, it also marks the fact that all of the surveys considered here are definitely complete out to this redshift.

Since this paper was submitted, SDSS DR14 spectra were made public (Abolfathi et al. 2017), including 810 Stripe 82X X-ray sources that did not previously have spectroscopic redshifts. This allowed a new test of the photometric redshifts for a population of fainter sources (the median *r*-band magnitude of this blind sample is 2 mag fainter than that of our training sample) with a systematically lower spectroscopic signal-to-noise ratio. We visually inspected all DR14 spectra reported in this work using Dwelly et al. (2017). For these 810 redshifts, we obtained $\sigma_{nmad} = 0.0626$, essentially the same as for the training and test data sets, and 19% outliers, which is higher than the 13.7% for the training set.

4.1. Variability

AGNs vary on timescales of hours to years. In Stripe 82, the SDSS survey includes 80–100 repeated images over a period of 3 yr, so it is sensitive to variability on timescales of months. Palanque-Delabrouille et al. (2011) used color cuts and morphology (point-like) from SDSS DR12 to select quasar-like objects from Stripe 82 and calculate their strength of variability using a neural network code. As all of our objects are not necessarily quasars, only 3052 of our X-ray objects (49%) overlap with their sample.

The neural network output parameter from Palanque-Delabrouille et al. (2011), *nnv*, which reflects the strength of quasar-like variability, varies between 0 and 1. (A value of −1 indicates that not enough epochs of data were available to draw reliable conclusions.) Most of these sources—2432 objects, which is 39% of our sample—have $nnv > 0.5$, meaning highly variable. Of these, 204 have extended morphology and are probably nearby Type 1 AGNs, while 2228 have point-like morphologies and thus could be variable stars or quasars. Unlike S09, we divided the variable sources according to their morphology. For the extended variable sources, we have spectra for 45 sources, and we achieved an outlier fraction of 29% and $\sigma_{nmad} = 0.0669$. For the point-like variable objects, we have spectra for 1013 sources, and we get 14.9% outliers and $\sigma_{nmad} = 0.0561$.

AGN variability can have an effect on the photometric redshifts, particularly when data at different wavelengths were obtained at different times. However, for the sources dominated by stellar light (3387 sources; 54.8% overall, of which 1044 objects, or 16.9%, are fainter than $r \gtrsim 22.5$ mag), AGN variability is unlikely to affect the photometric redshifts. For the most luminous AGNs (2329 objects; 37.7%), variability can affect the shape of the SED, but most of these (1216 objects; 19.7%) have spectroscopic redshifts. So at most, AGN variability could affect up to 1113 objects (18% of the sample);

Table 9
Outlier Fractions for Different Soft Flux Cuts[a]

Object Type	$F_{0.5-2\,\mathrm{keV}} > 10^{-14}$ erg cm^{-2} s^{-1}	$F_{0.5-2\,\mathrm{keV}} > 3.5 \times 10^{-14}$ erg cm^{-2} s^{-1}	$F_{0.5-2\,\mathrm{keV}} > 10^{-13}$ erg cm^{-2} s^{-1}
Point-like	16.4% outlier $\sigma_{\mathrm{nmad}} = 0.0605$ 695 objects	25.5% outlier $\sigma_{\mathrm{nmad}} = 0.0665$ 149 objects	34.3% outlier $\sigma_{\mathrm{nmad}} = 0.0822$ 29 objects
Extended	9.8% outlier $\sigma_{\mathrm{nmad}} = 0.0619$ 193 objects	4.3% outlier $\sigma_{\mathrm{nmad}} = 0.0555$ 69 objects	0% outlier $\sigma_{\mathrm{nmad}} = 0.0633$ 20 objects

Note.
[a] Only for objects without bright nearby neighbors.

Table 10
Comparison to Photometric Redshifts in the Literature for Sources Overlapping with Our Work[a]

Photoz Catalog	Source Counts	Outliers	σ_{nmad}
Peters et al. (2015; Quasars)	565	16.11%	0.0475
This work		10.8%	0.0529
Richards et al. (2015; Quasars)	920	6.8%	0.0236
This work		16%	0.0601
Bovy et al. (2012; Quasars)	945	8.15%	0.0312
This work		13.76%	0.0559

Note.
[a] The values of σ_{nmad} and fraction of outliers are from a comparison of photometric and spectroscopic redshifts for the sources common to both works.

of these, 471 (7.6%) have $nnv > 0.5$ and 188 (3%) do not have sufficient information to calculate nnv. These sources can be easily identified in the final catalog.

4.2. Comparison with Other Fields Using This Approach for Photometric Redshifts

Table 8 compares the quality of our photometric redshifts with those in other X-ray surveys. Not surprisingly, the surveys with intermediate-band or narrowband photometry generally have more accurate photometric redshifts and fewer outliers, because narrowband photometry can easily detect the emission lines of the galaxy component. In addition, narrowband and intermediate-band photometry fills the gaps between the broadband filters. This allows the detection of characteristic features like the 4000 Å and Lyα breaks that can be missed in broadband photometry.

Our results are most similar to the Fotopoulou et al. (2012) results for the Lockman Hole, where only a limited number of broadband filters was used. Our results are slightly better due to a template library that is better optimized for bright AGNs. It is worth noting that, contrary to other surveys, the published photometry for Stripe 82X was not analyzed homogeneously, as explained in Section 3.4. Reprocessing the data uniformly across multiwavelength catalogs—in particular, defining consistent total magnitudes—would likely reduce the photometric uncertainties and thus improve the accuracy of the photometric redshifts.

4.3. Soft X-Ray Flux and Photometric Redshift Accuracy

This is the first photometric redshift study of a large, bright, X-ray-selected AGN sample. In particular, this is the largest investigation of AGN-appropriate templates for sources with $F_{0.5-2\,\mathrm{keV}} > 10^{-14}$ erg cm^{-2} (38%; 2426 objects). The well-studied pencil-beam surveys have far fewer objects at these bright fluxes; for example, CDFS has seven sources (1%) and AEGIS has 22 sources (2%) brighter than this limit. Even *XMM*-COSMOS, with 2 deg^2 of coverage, has only 221 (6%) sources of this type. We need to quantify the fitting quality at these bright fluxes, because a point-like object with high soft flux is most likely a quasar with a nearly perfect power-law spectrum. Such SEDs lack features such as the 4000 Å break, which are important for template fitting. As such, we expect that our results should deteriorate with increasing soft X-ray flux.

We tested the accuracy of photometric redshifts for three X-ray bins brighter than this limit, as shown in Figure 13 and summarized in Table 9. For point-like objects, the fraction of outliers and σ_{nmad} increases for higher soft flux samples, while the opposite happens for extended samples. This is likely because the X-ray-brightest extended objects are nearby and their SEDs are dominated by host galaxy light, whereas the brightest point-like objects are quasars dominated by pure power laws. Note that it is the outlier fraction that sees the biggest change with flux limit; the accuracy of the photometric redshifts changes much less because it is the median value.

4.4. Comparisons with Other Methods Of Calculating Photometric Redshift

Since Stripe 82 is fully covered by SDSS, others have calculated photometric redshifts for subsets of optically or spectroscopically selected quasars using a variety of techniques. Here we compare results for the Stripe 82X sources that are in common with those studies, as summarized in Table 10. The samples that exclusively select quasars from optical data are expected to (and in some cases do) perform better than our approach. This is because of the difference in population type: our sample includes Type 1 and Type 2 AGNs, starburst galaxies, and some spiral and elliptical galaxies. The diversity in object type requires a large number of models in our template library, which leads to degeneracy and increases our outlier numbers and inaccuracy.

Bovy et al. (2012; hereafter the XDQSO model) uses spectroscopically confirmed quasars from SDSS DR7 with $z > 0.3$ to model the color–redshift relationship. The XDQSO model uses this color–redshift relationship, along with an apparent magnitude–dependent redshift prior, to calculate a probability distribution of photometric redshift for each object. They found accurate photometric redshifts ($|\triangle z| < 0.3$) for 97% of the quasars (we do not have their spectroscopic sample available to calculate η and σ_{nmad}). There are 945 objects in the Stripe 82X sample that overlap with the XDQSO work and also have spectra, so we compared our results.

Peters et al. (2015) used a Bayesian technique to select quasar candidates from SDSS and Stripe 82 and used the method described in Weinstein et al. (2004) to find photometric redshifts for these objects. This work also optically selects quasars only. This approach uses astrometric parameters and optical photometry and reaches an accuracy of $|\triangle z| < 0.3$ for

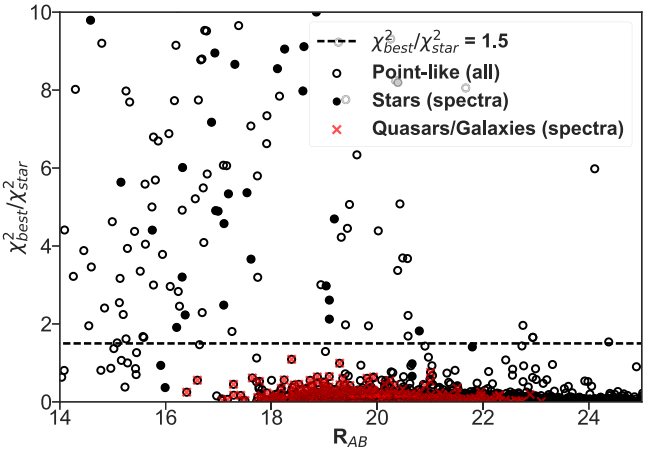

Figure 14. Ratio of χ^2 values for best-fit quasar/galaxy model ($\chi^2_{\rm best}$) to best-fit star ($\chi^2_{\rm star}$) against $R_{\rm AB}$ magnitude. Low ratios indicate secure quasar/galaxy identifications; red crosses show spectroscopically confirmed quasar/AGNs. Black filled points show spectroscopically confirmed stars, only five of which (all cataclysmic variables) have ratios <1.5 and thus are misclassified (10% of the 57 stars with spectra).

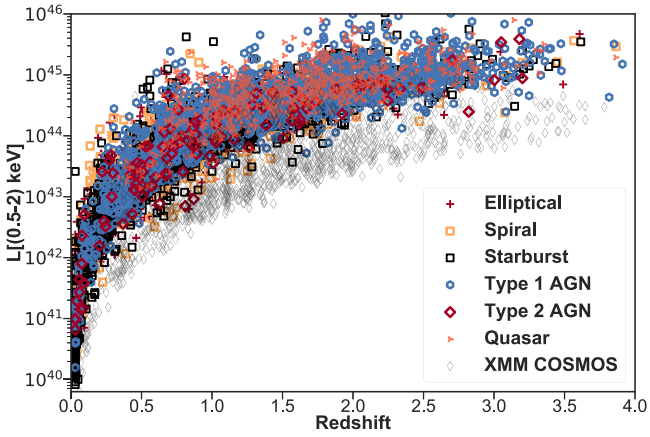

Figure 15. X-ray luminosity vs. redshift for X-ray sources in Stripe 82X and *XMM*-COSMOS. Because of their larger volume, the Stripe 82X AGNs/quasars are more luminous than the *XMM*-COSMOS AGNs. The Type 1 AGNs/quasars in the Stripe 82X sample are the brightest class of objects in the X-ray, as expected, and stars line up at the bottom of the distribution. The *XMM*-COSMOS objects are less luminous in the X-ray.

Table 11
Comparison of the Accuracy of the SED Fitting Method and Color–Color Method for Identifying Stars for Objects with Spectra

Classification Type	SED	Color
Stars correctly classified	52	25
Stars misclassified as extragalactic	5	18
Extragalactic objects misclassified as stars	0	0

76.9% of the quasars. Using the spectroscopic sample of that work, this translates to $\eta = 23.3\%$ and $\sigma_{\rm nmad} = 0.035$.

Richards et al. (2015) used the same approach as Peters et al. (2015) but with more bands (adding *GALEX* and IRAC to the SDSS, VHS, and AllWISE data). More bands improves results: this work has an accuracy of $|\Delta z| < 0.3$ 93% of the time (when NIR is present), which translates to $\eta = 7.03\%$ and $\sigma_{\rm nmad} = 0.018$ for the entire spectroscopic sample of that work.

A machine-learning approach to calculate SDSS quasar luminosity was taken by Brescia et al. (2013). However, the spectroscopic redshifts used to train the data were from SDSS DR7, and, while trying to compare our results, we found that with the updated pipeline in SDSS DR12/DR13, many of these objects have changed spectroscopic redshift. As a consequence, our results were not comparable.

4.5. Identification of Stars and Comparison with Color-based Star Identification

Following the method explained in S09, we identified stars by SED fitting using the following criteria on point-like sources: $\chi^2_{\rm best} \geqslant 1.5 \times \chi^2_{\rm star}$. Here $\chi^2_{\rm best}$ corresponds to the χ^2 value returned by the best-fit AGN/galaxy template, and $\chi^2_{\rm star}$ corresponds to the best-fit star template. The appropriate multiplicative factor depends on photometry and usually falls between 1 and 2. Figure 14 compares the quality of fit for galaxy/quasar and stellar templates. The spectroscopically confirmed AGNs are shown as red points, all of which fall below a ratio of 1.5.

Generally, if a star has a close neighbor, it could mistakenly be classified as extended, in which case a galaxy template will fit about as well as the stellar template. This is the biggest cause of misclassification of stars. Truly point-like objects can easily be distinguished as stars or AGNs/quasars, as shown in Figure 8 (and confirmed by their spectra).

To investigate if we can improve the accuracy of classification, we looked into a color-based method of stellar identification presented in LaMassa et al. (2016a): $R - W1 = (0.998 \pm 0.02)(R - K) + 0.18$, where all magnitudes are in the Vega magnitude system. We found that the SED fitting method is more accurate in correctly identifying stars based on objects for which we have spectroscopic information. We summarize our findings in Table 11.

One caveat of finding stars using template fitting is that if the object is misclassified as extended due to close nearby neighbors, we use incorrect priors and cannot correctly classify such objects. Scranton et al. (2002) discussed some challenges that arise in morphological classification due to close nearby neighbors. We found five cases where a close nearby object causes a star to appear extended. These stars were misclassified into the extended sample. Without better-resolution data, we cannot correct for nearby neighbors distorting FWHM information. Nearby elliptical galaxies are very well fitted by stellar templates, so we cannot apply the $\chi^2_{\rm best}/\chi^2_{\rm star} > 1.5$ threshold on the extended sample without misclassifying a lot of galaxies as stars. This is why we search for stars only among the point-like sources. One of these five stars is recognized as a star by the color–color test, one is miscategorized as "extragalactic," and, for the rest, we do not have color diagnostic information.

4.6. Characterization of the Sources

As we discussed in Section 1, Stripe 82X provides information on a population that was barely represented in COSMOS due to its smaller volume. Figure 15 shows the luminosity–redshift distributions of these two surveys, demonstrating that the larger Stripe 82X volume samples ~15 times higher luminosities.

Template fitting gives us a rough idea of the demographics of the Stripe 82 X-ray sources. Table 12 presents numbers of each type of object based on the best-fit SED template. Of course, since most of the "galaxies" have X-ray luminosities in excess of $10^{42.5}$ erg s^{-1}, these are really obscured AGNs.

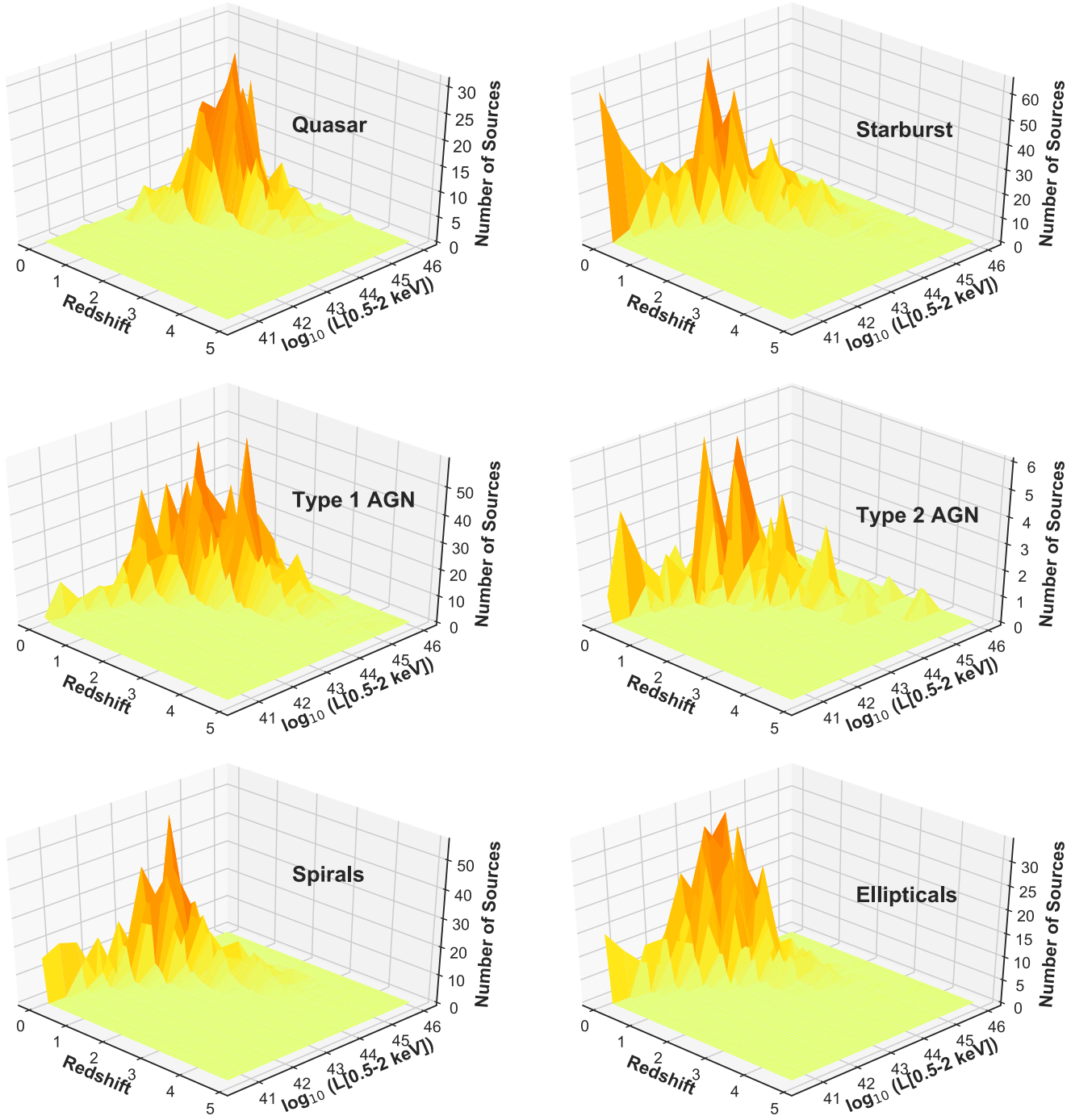

Figure 16. Luminosity and redshift distribution of (top left) quasars (QSOs), (top right) starbursts, (middle left) Type 1 AGNs, (middle right) Type 2 AGNs, (bottom left) spiral galaxies, and (bottom right) elliptical galaxies in the Stripe 82X survey using the best-fit SED templates.

Table 12
Comparison of the Accuracy of the SED Fitting Method and Color–Color Method for Identifying Stars for Objects with Spectra

Best-fit SED Type	Template Number	Description	Number of Objects
Stars	$\chi^2_{\rm best} \geqslant 1.5 \times \chi^2_{\rm star}$	As explained in Section 4.5	230 (3.7%)
Ellipticals	33–35 (From Table 5)	Elliptical galaxies	797 (12.9%; 4 at $z > 3$)
Spirals	14, 36–40	Spiral galaxies	1000 (16.2%; 6 at $z > 3$)
Starbursts	1, 2, 13, 25, 26, 29–32	M82, Mrk231, I22491-Type 1 hybrids with $> = 50\%$ I22491 contributions	1474 (23.8%; 24 at $z > 3$)
Type 2	15–24	Any Type 2 hybrid	123 (2%; 9 at $z > 3$)
Type 1 hybrid	5–12, 27, 28	Type 1 hybrids with >50% Type 1 contribution	1655 (26.8%; 56 at $z > 3$)
High-luminosity quasar	2, 3	100% quasars	682 (11%; 17 at $z > 3$)
Total			5961 (96.4%; 114 at $z > 3$)

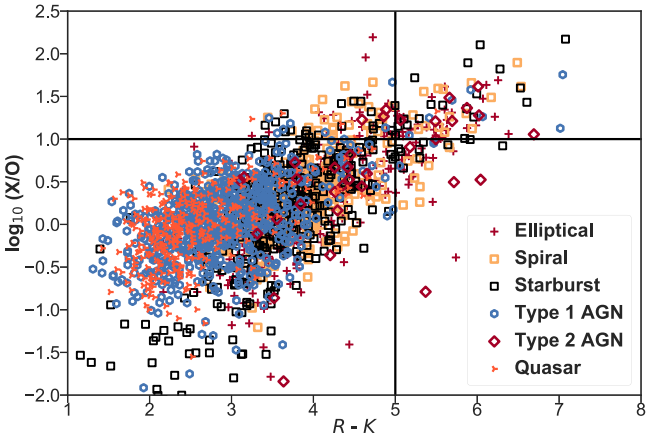

Figure 17. Log of ratio of hardband X-ray flux to *r*-band flux plotted against *R*–*K* Vega magnitude. Objects with $\log(X/O) > 1$ and $R–K > 5$ are candidates for heavily obscured AGNs; most of the 82 objects that fit these criteria have SEDs best fit by starburst, spiral, elliptical, and Type 2 templates (see the legend for symbols), as expected for obscured AGNs.

Together with the explicitly identified Type 2s, obscured AGNs make up roughly one-third of the extragalactic objects. The observed ratio of Type 2 to Type 1 AGNs is roughly 4:5; the intrinsic ratio can be much higher, because obscured AGNs are fainter than unobscured AGNs (for the same underlying luminosity). In Figure 16, we present the overall distribution in luminosity and redshift for each type of object.

The most interesting question is whether there are many obscured sources at high luminosity. Following Brusa et al. (2010), we look for an obscured population using *R*–*K* Vega magnitudes and the 2–10 keV X-ray–to–*r*-band flux ratio (X/O), as shown in Figure 17. Objects with $\log(X/O) > 1$ and $R–K > 5$ are obscured AGN candidates. In the Stripe 82X sample, 368 objects have $\log(X/O) > 1$. Of the 368 objects, 78 also have $(R–K)_{\rm Vega} > 5$ ($\sim$2.5 deg^{-2}), and their SEDs are well fitted by starburst, spiral, elliptical, and Type 2 templates, consistent with what we expect for heavily obscured AGNs/quasars.

For comparison, Brusa et al. (2010) found 105 objects in this region of color–color space in the *XMM*-COSMOS survey ($\sim$52.5 deg^{-2}). Nine of our 78 candidate obscured objects have redshift $z > 2$, and one has redshift $z > 3$; independent of color, 815 (129) objects have $z > 2$ ($z > 3$). Of the 129 sources (2% of the entire sample) that have redshift $z > 3$, only 32 (<1%) are spectroscopically confirmed. Among the 97 without spectroscopic confirmation, only 25 have PDZ > 90% and can be considered reliable. The low PDZ of the remaining sources is due to the limited number of photometric points and/or their large photometric errors.

Using slightly different criteria, Perola et al. (2004) and Civano et al. (2005) found that objects with $\log(X/O) > 1$ and $F_{(2-10)\,\rm keV} \geqslant 10^{-14}$ erg (cm^2 s)$^{-1}$ are high-luminosity obscured quasar candidates. Of the Stripe 82X sources, 375 meet these criteria (11.981 deg^{-2}). We have a dedicated spectroscopic follow-up program targeting candidate obscured quasars (LaMassa et al., submitted), and we are focusing particularly on obscured and/or high-redshift candidates.

Finally, we report the total distribution of photometric redshifts and X-ray full-band luminosities (0.5–10 keV) by taking into account the probability distribution of redshifts for each object, and not just the best-fit value, in Figures 18 and 19, respectively. Typical probability distributions of the redshift of individual objects look similar to the bottom panels of Figure 8. The total redshift distribution as shown in Figure 18 was calculated by summing over the probability distributions of all objects.

As expected, the Stripe 82X luminosity distribution is skewed to higher luminosities, as shown in Figure 19 (calculated using the full photometric redshift probability distributions). These probability distributions of individual objects can also be used to derive luminosity functions, clustering, and other redshift-dependent results, as shown by Allevato et al. (2016), which will be the subject of future work.

5. Conclusion

We fitted SED templates to 5961 X-ray objects (96.4%) in the Stripe 82X survey (LaMassa et al. 2013a, 2013b, LM16) and calculated photometric redshifts with an outlier fraction of 13.69% and a $\sigma_{\rm nmad}$ of 0.06. This is the largest-volume X-ray survey to date for which photometric redshifts have been calculated, and as such, it has given us important insights, such as optimizing template selection for the higher-flux population found in large-area, shallow surveys. We have described our attempts to identify a set of templates that would be representative of all objects but small enough in size to minimize degeneracy. These template libraries may be a helpful starting point for other large-volume surveys that would require photometric redshifts, such as XXL (Menzel et al. 2016; Pierre et al. 2016), 3*XMM* (Rosen et al. 2016), *eROSITA* (Merloni et al. 2012), and LSST (Ivezic et al. 2008).

With this paper, we release a catalog containing information about the X-ray sources, their correct associations with the multiwavelength ancillary data, the multiwavelength photometry used for template fitting, visually inspected spectroscopic redshifts, variability information, and photometric redshifts, including the $P(z)$ probability distributions. We also provide cutout images at various bands, the best-fit SED model (as in Figure 8) for each source, and new libraries of SEDs optimized for wide and shallow X-ray surveys.

We find that in the case of point-like objects, 18% of the outliers have a secondary redshift that is very close to the spectroscopic redshifts of those objects. This lends support to the argument that a more accurate approach in using photometric redshifts is to consider the probability distribution of redshifts for one object, rather than just one best-fit value (e.g., Georgakakis et al. 2014; Buchner et al. 2015; Miyaji et al. 2015).

We were able to determine that most outliers tend to have important spectral features, such as the 4000 Å break and Lyα break, that fall in between filter response curves or in the UV region, where we do not have data for 80% of the sources. We also found that we have comparable/slightly better results than other studies that only have broadband data, possibly because our library contains more Type 1 templates. Accuracies can be improved significantly when at least some narrowband or intermediate-band filters are present.

One interesting result of the study is that for point-like objects that are bright in the soft X-ray band ($>1e^{-13}$ erg cm^{-2} s^{-1}), we get a large fraction of outliers ($\sim$33%). The point-like morphology and high soft flux indicate that these objects are luminous unobscured quasars. Without the ability to see strong emission lines with narrowband or intermediate-band

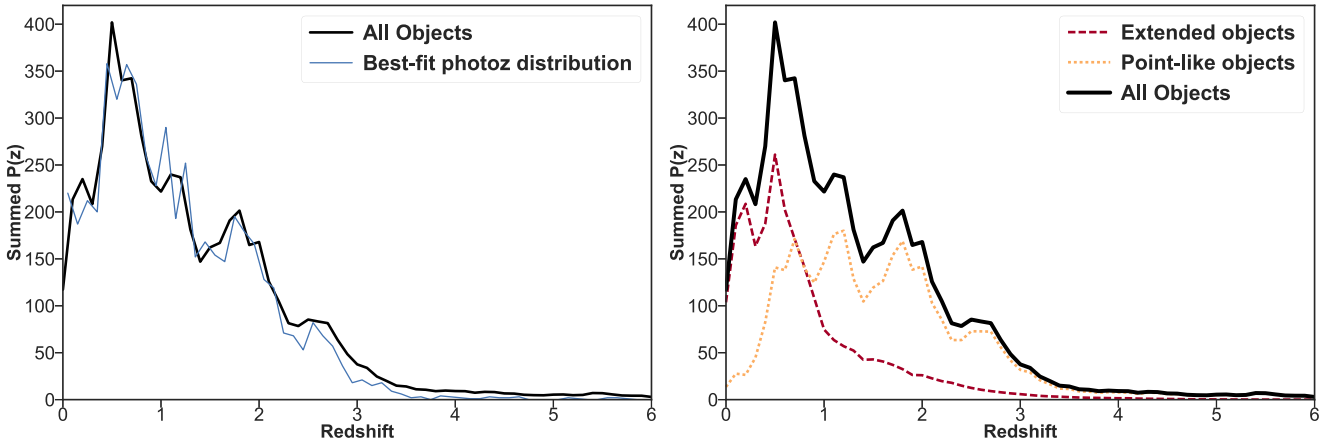

Figure 18. Summing the normalized probability distributions of photometric redshifts for each object. The probability distribution, $P(z)$, for each object is described in Equation (4). The left panel shows how the summed $P(z)$ compares to the distribution of best-fit photometric redshifts, and the right panel shows the summed $P(z)$ of all objects, along with the contribution of extended and point-like fractions.

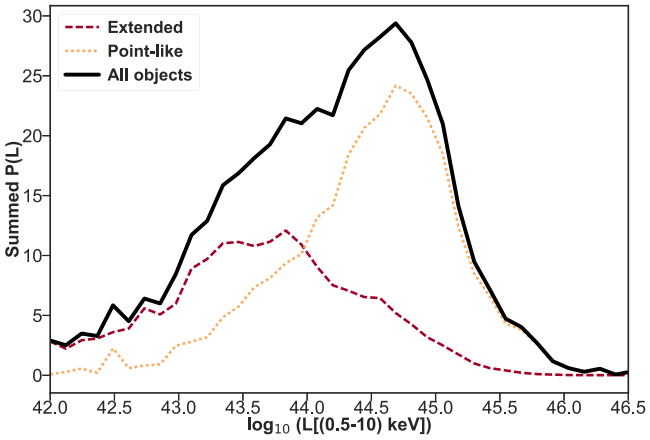

Figure 19. X-ray full-band luminosity (0.5–10 keV) distribution by taking into account the normalized probability distribution of the photometric redshift of each object.

filters, it is difficult to get the correct redshift for such objects using template fitting. As for relatively X-ray-bright objects below $1e^{-13}$ erg cm^{-2} s^{-1}, the template libraries presented in this work should be appropriate for fields with similar depth.

This work can be improved if intermediate-band or narrowband photometry becomes available for the region or with deeper optical photometry (e.g., HyperSuprimeCam imaging). Higher-resolution imaging would be useful for better distinguishing between point-like and extended samples.

We are very grateful to the anonymous referee for a careful reading of this work and providing comments that helped us improve a number of areas that were not sufficiently clear in our first submission.

TA wishes to thank her parents, M. A. Quayum and Shamim Ara Begum, and her husband, Mehrab Bakhtiar, for their constant support under all conditions. She is very grateful to Ms. Birgit Boller of Max Planck, Garching, for supporting her visit there. The authors thank Ms. Geriana Van Atta of Yale University. This project was supported by Yale University, and the *XMM-Newton* analysis was partially supported by NASA grant NNX15AJ40G.

Software: Astropy (Astropy Collaboration et al. 2013), Matplotlib (Hunter 2007), Topcat (Taylor 2005), STILTS (Taylor 2006).

Appendix A
Output Catalog Columns

The final catalog can be downloaded from https://yale.app.box.com/s/6o4dtks5tmxuq7j083s0wujf2ke8slvx and is available in the online version of Table 13 in this article. Descriptions of the output table columns are in this section. Note that this catalog supersedes that of LM16, because we explicitly resolved conflicting identifications (previously left to the reader) and used deeper optical and MIR catalogs. All null values are set to −99, except for num_filt, morphology, luminosity, and luminosity distances (both photometric and spectroscopic), which are set to 0, and duplication_id_1 and duplication_id_2, which are set to 9999999. There is a special case of W3 and W4 errors that are sometimes left blank, as explained in Table 13.

Appendix B
Selecting Template SEDs

One example of minimizing a library is discussed here. Ideally, when constructing a library, we need to make sure that all types of sources are represented. However, an excessive number of templates applied to sources with a SED defined by a limited number of photometric points introduces degeneracies in the redshift solution. Thus, the compromise is to make sure that key SED features are represented in the library, keeping the number of templates as small as possible. In this way, even if the template is not exactly the best template fitting the data, it is sufficiently close for allowing a reliable redshift determination.

For the extended-objects sample, the template shown in red in Figure 20 (left) closely fits most of the objects that are well fitted by the I22491 hybrids (plotted below the red template), although it produces an inaccurate redshift, as shown in Figure 20 (right). The horizontal line at $z_{\rm phot} \sim 0.39$ is caused by this template. The photometric redshift code is very dependent on sharp features in the spectra, such as the Lyα break. Therefore, the degeneracy is not surprising, because the I22491 hybrids and this red template have many of the same features. However, some very low-redshift objects that appear in a horizontal line at $z_{\rm phot} \simeq 0.03$ in Figure 11 (right) are better fitted by the red template. This template was not included in the final library, because the photometric redshifts of those low-redshift objects are within acceptable $\sigma_{\rm nmad}$ without it and

Table 13
Column Descriptions of Final Output Table

Column	Description
Rec_no	ID number for each source as assigned in LM16
X-ray data:	
Catalog	Name of the original X-ray survey from LM16 (AO10, AO13, *Chandra*, or archival *XMM*)
Xray RA, DEC, RA_DEC_ERR	R.A., decl., and error in position of the X-ray source
Soft_flux	X-ray flux in 0.5–2 keV band
Soft_detml	Significance of detection in 0.5–2 keV band: detml $= -\ln P_{\rm random}$
Hard_flux	X-ray flux in 2–10 keV band
Full_flux	Total X-ray flux in 0.5–10 keV band
Association data:	
Association	This field indicates how many catalogs agree that the association we selected for the X-ray object is the correct association. "Sp," "Sh," "V," "F," and "J" stand for SpIES, SHELA, VHS, and SDSS and coadded catalogs FT16 and J14, respectively. "SpVJr" indicates that IRAC, VHS, and J14 *r* band agree and there is no conflict with the association of this X-ray object. "V" might indicate that we only have VHS data for this object or that we found a VHS counterpart to be the most likely counterpart. LM16 indicates that these sources were added from the LM16 catalog—we did not find them through our MLE matches, but these sources exist in SDSS DR13 in at least one single-epoch frame. Details of how we arrived at these results are discussed in Section 2.5.
RADEC_from	When we select R.A. and decl. for the best X-ray association, we look at all the catalogs that agree and choose coordinates from the one with the best astrometric accuracy (SDSS, than VHS, than IRAC).
CTP_RA, CTP_DEC	R.A. and decl. of the best associations for the X-ray object
QF	Quality flag: this field indicates whether or not there was a conflict in association. Described in detail in Figure 6.
Xray_ctp_dist	Distance (in arcseconds) between X-ray coordinates and counterparts
SDSS_rel_class, VHS_rel_class, IRAC_rel_class	Reliability class (Secure/Ambiguous/Sub-threshold) for SDSS, VHS, and IRAC counterparts, respectively
Manual_Check	For each visually checked source (all sources with conflicting associations), we added a manual comment describing the issue that might lead to difficulty in counterpart identification or photometry contamination. Some examples: "2150: two very close sources," "2152: extended source, so SpIES coordinate is a little off," "2155: looks like one very bright source in optical and one bright and one nearby faint source in SpIES"
Photometric data:	
mag_fuv, magerr_fuv, mag_nuv, magerr_nuv	Extinction-corrected *GALEX* FUV and NUV SEXTRACTOR AUTO magnitude and magnitude errors; all magnitudes are in the AB system
u, uerr, g, gerr, r, rerr, i, ierr, z, zerr	SDSS coadded (SEXTRACTOR AUTO) magnitudes and corresponding errors. If the field "Coadded" is set to "FT16," the data come from FT16, and if it is set to "J14," the photometry comes from J14. We allow all photometry data from the former catalog, and when no photometry is available, we look at the latter and take all data with SEXTRACTOR flags set to 0 or 2. We tried to correct for galactic extinction whenever extinction information was available. If extinction was not available, sdss_ext_corr is set to "N/A."
j, jerr, h, herr, k, kerr	Extinction-corrected magnitudes and magnitude errors from the VISTA VHS survey in the *J, H*, and *K* bands (2.″8 and 5.″6 radius aperture magnitude for point-like and extended sources, respectively)
juk, juk_err, huk, huk_err, kuk, kuk_err	Extinction-corrected magnitudes from the UKIDSS Large Area Survey catalog in the *J, H*, and *K* bands (2.″8 and 5.″6 aperture magnitude for point-like and extended sources, respectively)
ch1_spies, ch1err_spies, ch2_spies, ch2err_spies	IRAC CH1 and CH2 data (SEXTRACTOR AUTO mag; not extinction-corrected) from Timlin et al. (2016).
ch1_shela, ch1err_shelas, ch2_shela, ch2err_shela	IRAC CH1 and CH2 (SEXTRACTOR AUTO mag) data (not extinction-corrected) from Papovich et al. (2016).
w1, w1err, w2, w2err, w3, w3err, w4, w4err	AllWISE (mpro) magnitudes and errors (not extinction-corrected). The W3 and W4 data appear later in the table (after the spectroscopic redshift data) because we do not use them to construct SEDs. The W3 and W4 magnitude errors are blank if the profile-fit magnitude is a 95% confidence upper limit or the source is not measurable (http://wise2.ipac.caltech.edu/docs/release/allwise/expsup/sec2_1a.html).
Context	LePhare needs this field to understand which filters to use to calculate photometry. For example, if we just need to use filters FUV (filter number 0), SDSS i (5), and CH1 SpIES (13), the context is set to $2^0 + 2^5 + 2^{13}$. In the catalogs, we use this column to indicate which bands we used for final template fitting by LePhare.
Spectroscopic data:	

Table 13
(Continued)

Column	Description
Redshift	Spectroscopic redshift
Redshift_Source	Source of spectroscopic data (e.g., SDSS DR13, DR12Q)
SPEC_class	Spectroscopic classification of this object
SPECOBJID	SDSS spectra object ID DR12Q, DR13, DR14
SPEC_subclass	Additional spectroscopic data on object type
Redshift_err	Spectroscopic redshift error
zwarning	Warning on redshift. Only ZWARNING = 0 was used in our training sample.
Photometry/variability flags:	
Fliri_flag	SEXTRACTOR extraction flag from FT16 catalog
EXT_CORR_FROM	The coadded SDSS catalogs do not come with extinction information. At the same time, if we can find an extinction match in SDSS DR7, this field is set to "SDSS." If we cannot, we use the EBV from the VHS catalog to calculate extinction, in which case this flag is set to "VHS."
artifact_fuv, artifact_nuv	*GALEX* artifact flags as described here: http://www.galex.caltech.edu/DATA/gr1_docs/GR1_Pipeline_and_advanced_data_description_v2.htm
fwhm_fuv, fwhm_nuv	FWHM for *GALEX* data, measured in pixels
Flags_nuv, Flags_fuv	SEXTRACTOR flags for NUV and FUV
*GALEX*_extended	*GALEX* object classification
*GALEX*_manflag	*GALEX* manual flag
u_fwhm, g_fwhm, r_fwhm, i_fwhm, z_fwhm	FWHM for each SDSS band from J14
nnv	Variability information for optical sources, varies from 0 to 1 (−1 for completely nonvarying sources)
VHS_mergedclass	Class flag from available measurements (1–0–1–2–3–9 = galaxy–noise–stellar–probableStar–probableGalaxy–saturated)
VHS_pstar, VHS_pgal	VHS pipeline probability that an object is a star or a galaxy, respectively
ch1_flag_spies, ch2_flag_spies, ch1_flag_shela, ch2_flag_shela	SEXTRACTOR flags for IRAC data
spies_class_star	SpIES object classification
high_rel1_spies, high_rel2_spies	Reliability of CH1 and CH2 SpIES (Timlin et al. 2016) data
XO	X-ray–to–optical ratio, as explained in Appendix C. This ratio is for X-ray hardband (0.5–2 keV) to SDSS *r* band.
Coadded	Indicates whether the photometry we use is from FT16 or J14. We prefer FT16 and use it when available.
Jiang_flag	J14 *r*-band SEXTRACTOR flag
Nearby_Neighbor_SEXTRACTOR	This is the remainder of the J14 SEXTRACTOR flag — 1 indicates that there is a nearby neighbor bright enough to significantly impact photometry. We exclude these objects from the training set.
Classification	Classification according to Figure 10
Photometric redshift data:	
Photoz	Best-fit photometric redshift
Photoz_best68_low, Photoz_best68_high	1σ lower and upper bound on photometric redshift, respectively
Chi_best	χ^2 value for our best-fit SED
Mod_best	Best-fit SED
Extlaw_Best	Extinction law used for best-fit SED (1 for Prevot et al. 1984 and 0 for none)
EBV_best	Color excess for host galaxy of AGN
PDZ_best	Described in Section 5. Can also be taken as LePhare's confidence on $z_{\rm phot}$.
Photoz_sec	Secondary redshift for SED with χ^2 value very close to best-fit χ^2 value
Chi_sec	χ^2 value for second-best fit
Mod_sec	SED for second-best fit
EBV_sec	Color excess used in second-best fit
PDZ_sec	Check Section 3
Chi_star	χ^2 value for best star template fit
Nband_used	Number of bands used by Lephare to determine $z_{\rm phot}$
Morphology	Morphology according to template fitting. 1: Stars, 2: Ellipticals, 3: Spirals, 4: Type 2, 5: Starbursts, 6: Type 1, 7: QSOs.
Color_morphology	LaMassa et al. (2016a) color morphology: extragalactic or star
SED_name	Name of the best-fit template
AstrometricJHK_2015_photoz	Peters et al. (2015) photoz
XDQSO_2012_photoz	Bovy et al. (2012) photoz
Richards_2015_photoz	Richards et al. (2015) photoz
Luminosity_distance_phot, Luminosity_distance_spec	Luminosity distance calculated using photoz and specz, respectively
Luminosity_phot, Luminosity_spec	Full-flux X-ray luminosity calculated using photoz and specz, respectively

Table 13
(Continued)

Column	Description
X-ray source duplication data:	
Duplication_flag	0: the object is unique. 1, −1: one of a duplicate pair of X-ray sources. We identify the same counterpart for both X-ray observations. 2, −2: duplicate pairs—these sources find different counterparts for X-ray sources. The positive flags (1, 2) indicate more reliable X-ray positions—we use only values of 0 or above to calculate outlier fractions/accuracy.
Duplication ID 1	REC NO of duplicate X-ray source
Duplication ID 2	Duplicate X-ray source REC NO if there is a second duplicate source

(This table is available in its entirety in FITS format.)

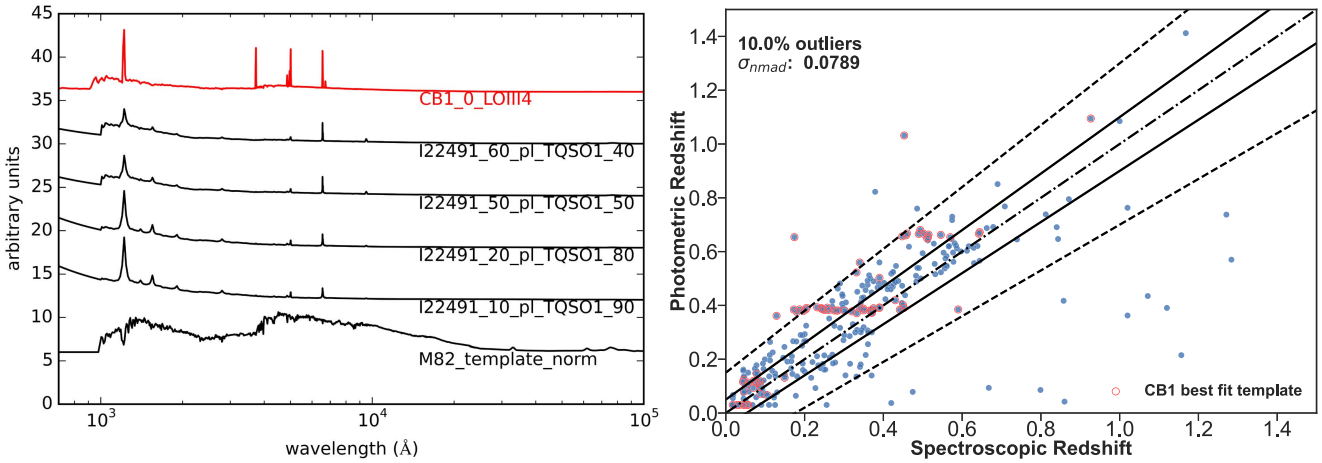

Figure 20. Left: All the templates in black are from the extended library. The red template is an extra SED that belongs to a young blue star-forming galaxy from Ilbert et al. (2009) and has sharp features similar to hybrids of I22491, also a starburst galaxy. The four templates below the red template are I22491 hybrids. Right: This figure shows an instance of degeneracy in fitting. The template library and objects used to fit are identical to those used to fit the objects in Figure 11 (right), with one exception: this library additionally contains the template indicated in red in the left image. This template has many of the same features as the I22491 starburst/type 1 QSO hybrids, so some objects that are more accurately fitted by I22491 are now degenerately fitted by the red template, giving rise to the horizontal line at $z_{\rm phot} \sim 0.39$ in this plot. Note that the addition of this template improves the fits for some very low-redshift objects ($z_{\rm spec} < 0.2$) that appear in a horizontal line in Figure 11 (right) at $z_{\rm phot} \sim 0.03$. So, we find that these horizontal lines are caused by template degeneracy. We cannot improve on this without increasing the inaccuracy of the overall work, so the optimum decision is to leave out the red template. Note that the objects that are in the $z_{\rm phot} \sim 0.03$ line have acceptable $\sigma_{\rm nmad}$, and the photometric redshifts calculated by this work are not largely different from the actual redshifts of these objects.

this template was causing bigger inaccuracies at higher redshifts.

It is not possible to remove templates when outliers are caused by essential models that accurately represent a significant fraction of the objects. For point-like objects, this work arrived at a smaller library than Salvato et al. (2009) and Hsu et al. (2014). But even with a small number of templates, the photometric data are not sufficient to avoid degeneracy entirely. This is shown in Figure 11, where some of the outliers (red squares) have secondary redshifts that are closer to the true spectroscopic redshifts.

Each template in the point-like library that causes outliers/degeneracy also produces the correct photometric redshifts for many other objects, so none can be removed. Note that these outliers with correct secondary redshifts demonstrate that it is more accurate to consider the entire probability distribution of redshifts for one object. Overall, the choice of templates was driven by the quality of the SED fits, the frequency of use of a particular template, and the absence of systematics in the redshift results when each template is used (see S09 and Hsu et al. 2014 for details).

Appendix C
X/O Conversions

To calculate X/O (introduced by Maccacaro et al. 1988) for our sample, we use soft flux (erg cm^{-2} s^{-1}) and SDSS i-band AB magnitude. We convert the i-band flux to the correct units as follows:

$$f_\nu = 3631 \times 10^{-\frac{m_{\rm AB}}{2.5}}\ {\rm Jy}. \quad (5)$$

To convert to f_λ:

$$f_\lambda = \frac{f_\nu}{3.34 \times 10^4}\left(\frac{\text{Å}}{\lambda}\right)^2 \frac{\rm erg}{\rm cm^2\ Å\ s}. \quad (6)$$

To get the total i-band flux, multiplying by the bandwidth of the i-band (1300 Å):

$$F_\lambda = \delta\lambda \text{Å} f_\lambda. \quad (7)$$

Taking the log of the flux:

$$\log_{10} F_\lambda = -\frac{m_{\rm AB}}{2.5} - 5.61425. \quad (8)$$

So X/O:

$$\log_{10}\left(\frac{F_{\rm X}}{F_{\lambda}}\right) = \log_{10}(F_{0.5-2\,\rm keV}) + \frac{m_{\rm AB}}{2.5} + 5.61425. \quad (9)$$

ORCID iDs

Mara Salvato https://orcid.org/0000-0001-7116-9303
Stephanie LaMassa https://orcid.org/0000-0002-5907-3330
C. Megan Urry https://orcid.org/0000-0002-0745-9792
Nico Cappelluti https://orcid.org/0000-0002-1697-186X
Carolin Cardamone https://orcid.org/0000-0003-4608-6340
Duncan Farrah https://orcid.org/0000-0003-1748-2010
Eilat Glikman https://orcid.org/0000-0003-0489-3750
Allison Kirkpatrick https://orcid.org/0000-0002-1306-1545
Giorgio Lanzuisi https://orcid.org/0000-0001-9094-0984
Stefano Marchesi https://orcid.org/0000-0001-5544-0749
Kirpal Nandra https://orcid.org/0000-0002-7150-9192
Priyamvada Natarajan https://orcid.org/0000-0002-5554-8896
Gordon T. Richards https://orcid.org/0000-0002-1061-1804
John Timlin https://orcid.org/0000-0001-8131-1801

References

Abolfathi, B., Aguado, D. S., Aguilar, G., et al. 2017, arXiv:1707.09322
Ahn, C. P., Alexandroff, R., Allende Prieto, C., et al. 2012, ApJS, 203, 21
Ahn, C. P., Alexandroff, R., Allende Prieto, C., et al. 2014, ApJS, 211, 17
Alexander, D. M., Bauer, F. E., Brandt, W. N., et al. 2003, AJ, 126, 539
Allevato, V., Civano, F., Finoguenov, A., et al. 2016, ApJ, 832, 70
Annis, J., Soares-Santos, M., Strauss, M. A., et al. 2014, ApJ, 794, 120
Arnouts, S., Cristiani, S., Moscardini, L., et al. 1999, MNRAS, 310, 540
Assef, R. J., Stern, D., Kochanek, C. S., et al. 2013, ApJ, 772, 26
Astropy Collaboration, Robitaille, T. P., Tollerud, E. J., et al. 2013, A&A, 558, A33
Aubourg, É., Bailey, S., Bautista, J. E., et al. 2015, PhRvD, 92, 123516
Barger, A. J., Cowie, L. L., Capak, P., et al. 2003, AJ, 126, 632
Battaglia, N., Leauthaud, A., Miyatake, H., et al. 2016, JCAP, 8, 013
Baumgartner, W. H., Tueller, J., Markwardt, C. B., et al. 2013, ApJS, 207, 19
Becker, R. H., White, R. L., & Helfand, D. J. 1995, ApJ, 450, 559
Bertin, E., & Arnouts, S. 1996, A&AS, 117, 393
Bovy, J., Myers, A. D., Hennawi, J. F., et al. 2012, ApJ, 749, 41
Brandt, W. N., & Hasinger, G. 2005, ARA&A, 43, 827
Brescia, M., Cavuoti, S., D'Abrusco, R., Longo, G., & Mercurio, A. 2013, ApJ, 772, 140
Brusa, M., Civano, F., Comastri, A., et al. 2010, ApJ, 716, 348
Brusa, M., Zamorani, G., Comastri, A., et al. 2007, ApJS, 172, 353
Buchner, J., Georgakakis, A., Nandra, K., et al. 2015, ApJ, 802, 89
Cappelluti, N., Brusa, M., Hasinger, G., et al. 2009, A&A, 497, 635
Cardamone, C. N., Urry, C. M., Damen, M., et al. 2008, ApJ, 680, 130
Cardamone, C. N., van Dokkum, P. G., Urry, C. M., et al. 2010, ApJS, 189, 270
Chiappetti, L., Clerc, N., Pacaud, F., et al. 2013, MNRAS, 429, 1652
Civano, F., Comastri, A., & Brusa, M. 2005, MNRAS, 358, 693
Civano, F., Elvis, M., Brusa, M., et al. 2012, ApJS, 201, 30
Civano, F., Marchesi, S., Comastri, A., et al. 2016, ApJ, 819, 62
Coil, A. L., Blanton, M. R., Burles, S. M., et al. 2011, ApJ, 741, 8
Comastri, A., Ranalli, P., Iwasawa, K., et al. 2011, A&A, 526, L9
Croom, S. M., Richards, G. T., Shanks, T., et al. 2009, MNRAS, 392, 19
Del Moro, A., Alexander, D. M., Bauer, F. E., et al. 2016, MNRAS, 456, 2105
Donley, J. L., Koekemoer, A. M., Brusa, M., et al. 2012, ApJ, 748, 142
Donley, J. L., Rieke, G. H., Alexander, D. M., Egami, E., & Pérez-González, P. G. 2010, ApJ, 719, 1393
Drinkwater, M. J., Jurek, R. J., Blake, C., et al. 2010, MNRAS, 401, 1429
Du, P., Hu, C., Lu, K.-X., et al. 2015, ApJ, 806, 22
Dwelly, T., Salvato, M., Merloni, A., et al. 2017, MNRAS, 469, 1065
Favole, G., Comparat, J., Prada, F., et al. 2016, MNRAS, 461, 3421
Fliri, J., & Trujillo, I. 2016, MNRAS, 456, 1359
Fotopoulou, S., Salvato, M., Hasinger, G., et al. 2012, ApJS, 198, 1
Garilli, B., Le Fèvre, O., Guzzo, L., et al. 2008, A&A, 486, 683
Georgakakis, A., & Nandra, K. 2011, MNRAS, 414, 992
Georgakakis, A., Pérez-González, P. G., Fanidakis, N., et al. 2014, MNRAS, 440, 339
Georgakakis, A., Salvato, M., Liu, Z., et al. 2017, arXiv:1704.08296
Gilli, R. 2004, AdSpR, 34, 2470
Guo, Y., Ferguson, H. C., Giavalisco, M., et al. 2013, ApJS, 207, 24
Hasinger, G., Cappelluti, N., Brunner, H., et al. 2007, ApJS, 172, 29
Hodge, J. A., Becker, R. H., White, R. L., Richards, G. T., & Zeimann, G. R. 2011, AJ, 142, 3
Hopkins, P. F., Hernquist, L., Cox, T. J., et al. 2006, ApJS, 163, 1
Hsu, L.-T., Salvato, M., Nandra, K., et al. 2014, ApJ, 796, 60
Hunter, J. D. 2007, CSE, 9, 90
Ilbert, O., Arnouts, S., McCracken, H. J., et al. 2006, A&A, 457, 841
Ilbert, O., Capak, P., Salvato, M., et al. 2009, ApJ, 690, 1236
Iovino, A., Petropoulou, V., Scodeggio, M., et al. 2016, A&A, 592, A78
Ivezic, Z., Tyson, J. A., Abel, B., et al. 2008, arXiv:0805.2366
Jiang, L., Fan, X., Bian, F., et al. 2014, ApJS, 213, 12
Jones, D. H., Read, M. A., Saunders, W., et al. 2009, MNRAS, 399, 683
Jones, D. H., Saunders, W., Colless, M., et al. 2004, MNRAS, 355, 747
Kirkpatrick, A., Pope, A., Charmandaris, V., et al. 2013, ApJ, 763, 123
Kirkpatrick, A., Pope, A., Sajina, A., et al. 2015, ApJ, 814, 9
Lacy, M., Storrie-Lombardi, L. J., Sajina, A., et al. 2004, ApJS, 154, 166
LaMassa, S. M., Civano, F., Brusa, M., et al. 2016a, ApJ, 818, 88
LaMassa, S. M., Urry, C. M., Cappelluti, N., et al. 2013a, MNRAS, 436, 3581
LaMassa, S. M., Urry, C. M., Cappelluti, N., et al. 2016b, ApJ, 817, 172
LaMassa, S. M., Urry, C. M., Glikman, E., et al. 2013b, MNRAS, 432, 1351
Lawrence, A., Warren, S. J., Almaini, O., et al. 2007, MNRAS, 379, 1599
Lehmer, B. D., Brandt, W. N., Alexander, D. M., et al. 2005, ApJS, 161, 21
Liu, Z., Merloni, A., Georgakakis, A., et al. 2016, MNRAS, 459, 1602
Luo, B., Brandt, W. N., Xue, Y. Q., et al. 2010, ApJS, 187, 560
Luo, B., Brandt, W. N., Xue, Y. Q., et al. 2017, ApJS, 228, 2
Maccacaro, T., Gioia, I. M., Wolter, A., Zamorani, G., & Stocke, J. T. 1988, ApJ, 326, 680
Marchesi, S., Civano, F., Elvis, M., et al. 2016, ApJ, 817, 34
Marconi, A., & Hunt, L. K. 2003, ApJL, 589, L21
Martin, D. C., Fanson, J., Schiminovich, D., et al. 2005, ApJL, 619, L1
McMahon, R. G., Banerji, M., Gonzalez, E., et al. 2013, Msngr, 154, 35
Mendez, A. J., Coil, A. L., Aird, J., et al. 2013, ApJ, 770, 40
Menzel, M.-L., Merloni, A., Georgakakis, A., et al. 2016, MNRAS, 457, 110
Merloni, A., Predehl, P., Becker, W., et al. 2012, arXiv:1209.3114
Miyaji, T., Hasinger, G., Salvato, M., et al. 2015, ApJ, 804, 104
Murray, S. S., Kenter, A., Forman, W. R., et al. 2005, ApJS, 161, 1
Nandra, K., Laird, E. S., Aird, J. A., et al. 2015, ApJS, 220, 10
Naylor, T., Broos, P. S., & Feigelson, E. D. 2013, ApJS, 209, 30
Newman, J. A., Cooper, M. C., Davis, M., et al. 2013, ApJS, 208, 5
Noll, S., Burgarella, D., Giovannoli, E., et al. 2009, A&A, 507, 1793
Palanque-Delabrouille, N., Yeche, C., Myers, A. D., et al. 2011, A&A, 530, A122
Papovich, C., Shipley, H. V., Mehrtens, N., et al. 2016, ApJS, 224, 28
Pâris, I., Petitjean, P., Ross, N. P., et al. 2017, A&A, 597, A79
Perola, G. C., Puccetti, S., Fiore, F., et al. 2004, A&A, 421, 491
Peters, C. M., Richards, G. T., Myers, A. D., et al. 2015, ApJ, 811, 95
Pierre, M., Chiappetti, L., Pacaud, F., et al. 2007, MNRAS, 382, 279
Pierre, M., Pacaud, F., Adami, C., et al. 2016, A&A, 592, A1
Prevot, M. L., Lequeux, J., Prevot, L., Maurice, E., & Rocca-Volmerange, B. 1984, A&A, 132, 389
Ricci, C., Ueda, Y., Koss, M. J., et al. 2015, ApJL, 815, L13
Richards, G. T., Myers, A. D., Peters, C. M., et al. 2015, ApJS, 219, 39
Rosen, S. R., Webb, N. A., Watson, M. G., et al. 2016, A&A, 590, A1
Rovilos, E., Fotopoulou, S., Salvato, M., et al. 2011, A&A, 529, A135
Rutledge, R. E., Brunner, R. J., Prince, T. A., & Lonsdale, C. 2000, ApJS, 131, 335
Salvato, M., Hasinger, G., Ilbert, O., et al. 2009, ApJ, 690, 1250
Salvato, M., Ilbert, O., Hasinger, G., et al. 2011, ApJ, 742, 61
Sanders, D. B., Soifer, B. T., Elias, J. H., et al. 1988, ApJ, 325, 74
Scranton, R., Johnston, D., Dodelson, S., et al. 2002, ApJ, 579, 48
SDSS Collaboration, Albareti, F. D., Allende Prieto, C., et al. 2016, arXiv:1608.02013
Sobral, D., Swinbank, A. M., Stott, J. P., et al. 2013, ApJ, 779, 139
Stern, D., Assef, R. J., Benford, D. J., et al. 2012, ApJ, 753, 30
Strauss, M. A., Weinberg, D. H., Lupton, R. H., et al. 2002, AJ, 124, 1810
Sutherland, W., & Saunders, W. 1992, MNRAS, 259, 413
Szokoly, G. P., Bergeron, J., Hasinger, G., et al. 2004, ApJS, 155, 271
Taylor, M. B. 2005, adass XIV, 347, 29
Taylor, M. B. 2006, adass XV, 351, 666

Timlin, J. D., Ross, N. P., Richards, G. T., et al. 2016, ApJS, 225, 1
Treister, E., Urry, C. M., Chatzichristou, E., et al. 2004, ApJ, 616, 123
Treister, E., Urry, C. M., & Virani, S. 2009, ApJ, 696, 110
Ueda, Y., Akiyama, M., Hasinger, G., Miyaji, T., & Watson, M. G. 2014, ApJ, 786, 104
van Dokkum, P. G., Whitaker, K. E., Brammer, G., et al. 2010, ApJ, 709, 1018
Viero, M. P., Asboth, V., Roseboom, I. G., et al. 2014, ApJS, 210, 22
Watson, M. G., Schröder, A. C., Fyfe, D., et al. 2009, A&A, 493, 339
Weinstein, M. A., Richards, G. T., Schneider, D. P., et al. 2004, ApJS, 155, 243
Xue, Y. Q., Luo, B., Brandt, W. N., et al. 2011, ApJS, 195, 10
Yu, Q., & Tremaine, S. 2002, MNRAS, 335, 965